Available online at www.sciencedirect.com
ScienceDirect
Journal of Computational Physics 227 (2008) 3824–3848
JOURNAL OF COMPUTATIONAL PHYSICS
www.elsevier.com/locate/jcp

Schwarz method for earthquake source dynamics

Lori Badea [a], Ioan R. Ionescu [b,1], Sylvie Wolf [b,*]

[a] Institute of Mathematics of the Romanian Academy, P.O. Box 1-764, RO 014700 Bucharest, Romania
[b] Laboratoire de Mathématiques, Université de Savoie, Campus Scientifique, 73376 Le Bourget-du-Lac Cedex, France

Received 1 July 2007; received in revised form 18 November 2007; accepted 23 November 2007
Available online 1 February 2008

Abstract

Dynamic faulting under slip-dependent friction in a linear elastic domain (in-plane and 3D configurations) is considered. The use of an implicit time-stepping scheme (Newmark method) allows much larger values of the time step than the critical CFL time step, and higher accuracy to handle the non-smoothness of the interface constitutive law (slip weakening friction).

The finite element form of the quasi-variational inequality is solved by a Schwarz domain decomposition method, by separating the inner nodes of the domain from the nodes on the fault. In this way, the quasi-variational inequality splits into two subproblems. The first one is a large linear system of equations, and its unknowns are related to the mesh nodes of the first subdomain (i.e. lying inside the domain). The unknowns of the second subproblem are the degrees of freedom of the mesh nodes of the second subdomain (i.e. lying on the domain boundary where the conditions of contact and friction are imposed). This nonlinear subproblem is solved by the same Schwarz algorithm, leading to some local nonlinear subproblems of a very small size.

Numerical experiments are performed to illustrate convergence in time and space, instability capturing, energy dissipation and the influence of normal stress variations. We have used the proposed numerical method to compute source dynamics phenomena on complex and realistic 2D fault models (branched fault systems).

MSC: 65M55; 65N55; 74L05; 74S05; 86A15; 86A17

Keywords: Domains with cracks; Slip-dependent friction; Wave equation; Earthquake initiation; Domain decomposition methods; Schwarz method

DOI of original article: 10.1016/j.jcp.2004.06.003
* Corresponding author. Present address: Laboratoire de Tectonique, CNRS UMR 7072 – Université Pierre et Marie Curie, Case 129, 4

E-mail addresses: Lori.Badea@imar.ro (L. Badea), ionescu@univ-savoie.fr (I.R. Ionescu), sylvie.wolf@free.fr (S. Wolf).
[1] Present address: Laboratoire des Propriétés Mécaniques et Thermodynamiques des Matériaux, CNRS UPR 9001 – Université Paris 13 – Institut Galilée, 99 avenue Jean-Baptiste Clément, 93430 Villetaneuse, France.

0021-9991/$ - see front matter © 2007 Elsevier Inc. All rights reserved.
doi:10.1016/j.jcp.2007.11.044

1. Introduction

Numerical modeling is an important tool to understand all three phases of earthquake source dynamics: initiation (also called nucleation), rupture propagation and arrest. The initiation phase of earthquakes, preceding the dynamic rupture, has been pointed out by detailed seismological observations [16,28] and some laboratory friction experiments, e.g. [40]. Theoretical studies [10,13,14,29,44], based on spectral analysis, have tried to give a qualitative description (characteristic time, critical fault length, etc.) of the initiation phase, which is characterized by an unstable evolution with an exponential growth in time of slip rate amplitude. Not all numerical schemes can capture this unstable behavior. For instance, a finite difference scheme was proposed in [29], for the anti-plane (2D, mode III) problem, and developed thereafter in [18,19] for the in-plane (2D, mode II) and 3D problems, but the use of a finite difference method restricts the applications on planar fault geometries. Further references on earthquake simulations can be bound for instance in [6]. We shall mention here a few recent works that constitute effective efforts to model realistic fault geometries. First, the possibility of including curved faults within a finite difference grid (here, the *rotated staggered grid*) is discussed in [11] and used to model 3D dynamic rupture along non-planar faults in [12]. Also, note that a finite volume technique is applied to rupture dynamics in [7]. The spectral element method (which is a special case of high order finite element method) is used in [20,21] to solve in-plane rupture dynamics. Finally, the boundary element method (BEM) – also known as boundary integral equation method (BIEM) – is widely used in this field, in 2D [30,42] as well as 3D [3,4].

There are much fewer finite element models [1,5,6,36] in the field of earthquake rupture simulation, because they are more difficult to implement than finite differences, and because low order schemes can lead to undesirable numerical dissipation. However, finite element methods have numerous advantages compared with finite differences. They can handle strong heterogeneities as well as complex geometries [6,37–39]. Besides, in dynamic contact mechanics, related friction laws are currently modeled using finite elements and there is a large number of papers and books on this topic (e.g. [27,31,33,34,47,48] and the references therein). The construction of solvers which exploit the locality of the friction law and simultaneously provide optimal solution methods is, although possible, far from trivial. We refer to [32] for scalar variational inequalities and, in particular, to [17] and the references cited therein for frictional contact problems. We believe that the comparison of the different finite element approaches (including spectral element methods) for dynamic rupture modelling should be discussed by means of a benchmark. Indeed, the differences between these methods are numerous: the finite elements can be of high order (SEM) or low order (P1 FEM); the time-stepping scheme can be fully explicit (mass lumping) or implicit (main characteristic of the method proposed in this paper); etc. Such a benchmark, which results could help us evaluate these differences and identify some others, is beyond the scope of the present paper.

Since the friction laws involved in dynamic faulting models are strongly nonlinear, the use of an implicit time-stepping scheme leads to a nonlinear elliptic problem at each time step. Domain decomposition is one of the efficient methods to solve this type of quasi-variational problem. The literature on domain decomposition methods is large. One can refer, for instance, to the papers in the proceedings of the annual conferences on domain decomposition methods (starting in 1988 [25]) or those cited in the books [35,41,43]. Naturally, most of the papers dealing with these methods address linear problems. Also, convergence proofs for variational inequalities are restricted, in general, to the inequalities coming from the minimization of quadratic functionals.

This article is a sequel to [6], which presented the first domain decomposition method to model dynamic faulting under slip-dependent friction in the anti-plane shearing configuration. Even if important features of the physical phenomenon (like stress interactions) are active in this configuration, only a limited number of geophysical faults are satisfactorily described by the anti-plane geometry. Moreover, in the anti-plane description of the friction phenomenon, the normal stress can be considered constant, which is a very important simplification. A remarkable consequence of this assumption is that we can associate the physical problem to the minimization of the energy function. By contrast, in the full 3D and in-plane configurations, studied in the present paper, the nonlinear problem at each time step cannot be associated to an optimization problem. This is due to the "non-associative" character of Coulomb friction law. The concept of associativity is currently used in the theory of plasticity when the flow rule can be written through the derivative of the yield

potential. Here, since the normal stress is involved in the friction law, the slip rate rule cannot be written through the derivative of the stress potential. Many important difficulties arise from the resolution of a quasi-variational problem instead of a variational problem, from both mathematical and computational points of view. However, the challenges in 3D modeling of earthquake source dynamics are worth the efforts of the present paper to overcome these difficulties.

The aim of this paper is to propose an efficient numerical scheme to model the initiation and propagation of rupture in a heterogeneous medium, on fault systems of complex geometry (in-plane or 3D) and heterogeneous frictional properties. Using a Schwarz method to solve the quasi-variational problem induced by an implicit time-stepping scheme, the original problem splits into two subproblems. The first subproblem is linear and its unknowns are the nodal values from the intact domain (i.e. excluding the faults). The unknowns of the second subproblem are the degrees of freedom of the mesh nodes lying on the faults, i.e. on the domain boundary where conditions of contact and friction are imposed. Evidently, this second subproblem is nonlinear; it is solved by the same Schwarz algorithm by splitting it into local nonlinear subproblems of a very small size (they have three unknowns in the in-plane problem and five unknowns in the 3D problem), so that quasi-explicit efficient solvers can be used. In fact, the resulting method is simply a nonlinear Gauss–Seidel method (see e.g. [24]) for the non-smooth subproblem, which exhibits a strongly local nonlinearity. Consequently, the solution procedure at each time step consists in the iterative resolution (until convergence) of one large linear subproblem and some very small nonlinear subproblems. The number of Schwarz iterations depends on the number of subdomains, hence on the number of nodes on the fault, which is always significantly smaller than the total mesh size.

The paper is organized as follows. In the next section, we formulate the continuous 3D problem as a quasi-variational inequality. Section 3 is devoted to the time discretization of the continuous problem using an implicit Newmark method. In Section 4, we describe the Schwarz algorithm developed to solve the finite element form of the discretized problem. In Section 5, we prove that the local nonlinear subproblems have a unique solution, and we give a detailed algorithm to solve them. An explicit formulation of these subproblems is derived in the Appendix. Section 6 is devoted to some numerical experiments. Some convergence tests are performed (instability capturing, energy dissipation). Also, normal stress variations on the fault are investigated, and the numerical method is applied to a relevant physical problem (behaviour of a branched fault system). Finally, in Section 7, the main points of this paper are summarized.

2. Continuous problem

We consider the deformation of an elastic body occupying, in the initial unconstrained configuration, a domain Ω in $\mathbb{R}^d$, where $d = 2$ for the plane case and $d = 3$ for the full 3D problem. The Lipschitz boundary $\partial\Omega$ of Ω is supposed to be smooth and divided into two disjoint parts: the exterior boundary $\Gamma_e = \partial\overline{\Omega}$ and the internal one Γ composed of N_f bounded connected surfaces (or arcs for $d = 2$) $\Gamma_f^i, i = 1, \ldots, N_f$, called cracks or faults. The exterior boundary consists of Γ_D and Γ_N. We denote by $\boldsymbol{n}$ the unit outward normal on Γ_e.

The elastodynamic problem consists in finding the displacement field $\boldsymbol{u} : [0, T] \times \Omega \to \mathbb{R}^d$ satisfying:

$$\mathrm{div}\boldsymbol{\sigma}(\boldsymbol{u}(t)) = \rho\ddot{\boldsymbol{u}}(t) \quad \text{in } \Omega, \tag{1}$$

$$\boldsymbol{\sigma}(\boldsymbol{u}(t)) = \mathcal{C}\boldsymbol{\varepsilon}(\boldsymbol{u}(t)) \quad \text{in } \Omega, \tag{2}$$

$$\boldsymbol{u}(t) = 0 \quad \text{on } \Gamma_D, \tag{3}$$

$$\boldsymbol{\sigma}(\boldsymbol{u}(t))\boldsymbol{n} = 0 \quad \text{on } \Gamma_N, \tag{4}$$

where $\rho > 0$ is the density and the dots represent time derivatives. The notation $\boldsymbol{\sigma}(\boldsymbol{u})$ denotes the stress tensor field lying in $\mathcal{S}_d$, the space of second order symmetric tensors on $\mathbb{R}^d$. The linearized strain tensor field is $\boldsymbol{\varepsilon}(\boldsymbol{u}) = (\nabla\boldsymbol{u} + \nabla^T\boldsymbol{u})/2$ and $\mathcal{C}$ is the fourth order symmetric and elliptic tensor of linear elasticity.

On Γ, we denote by $[\ ]$ the jump across Γ (i.e. $[w] = w^+ - w^-$), and the corresponding unit normal $\boldsymbol{n}$ on Γ points outwards the positive side. Afterwards we adopt the following notation for any displacement field $\boldsymbol{u}$ and for any density of surface forces $\boldsymbol{\sigma n}$ defined on Γ:

$$\boldsymbol{u} = u_n\boldsymbol{n} + \boldsymbol{u}_t \quad \text{and} \quad \boldsymbol{\sigma n} = \sigma_n\boldsymbol{n} + \boldsymbol{\sigma}_t,$$

where $u_n =: \boldsymbol{u}\cdot\boldsymbol{n}$ and $\boldsymbol{u}_t$ are the normal and tangential displacements, and $\sigma_n =: \boldsymbol{\sigma}(\boldsymbol{u})\boldsymbol{n}\cdot\boldsymbol{n}$ and $\boldsymbol{\sigma}_t$ are the normal and tangential over-stresses acting on Γ.

The contact on Γ is assumed to be frictional, without separation, and the stick and slip zones are not known in advance:

$$[\dot{u}_n(t)] = 0, \quad [\boldsymbol{\sigma}(\boldsymbol{u}(t))\boldsymbol{n}] = 0, \tag{5}$$

$$\begin{cases} [\dot{\boldsymbol{u}}_t(t)] = 0 \Rightarrow |\boldsymbol{\sigma}_t(\boldsymbol{u}(t)) + \boldsymbol{\sigma}_t^{\mathrm{p}}| \leqslant -\mu(s(t))(\sigma_n(\boldsymbol{u}(t)) + \sigma_n^{\mathrm{p}}), \\ [\dot{\boldsymbol{u}}_t(t)] \neq 0 \Rightarrow \boldsymbol{\sigma}_t(\boldsymbol{u}(t)) + \boldsymbol{\sigma}_t^{\mathrm{p}} = \mu(s(t))(\sigma_n(\boldsymbol{u}(t)) + \sigma_n^{\mathrm{p}})\frac{[\dot{\boldsymbol{u}}_t(t)]}{|[\dot{\boldsymbol{u}}_t(t)]|}, \end{cases} \tag{6}$$

where $\boldsymbol{\sigma}^{\mathrm{p}}$ is the pre-stress which will be supposed to be continuous on $\overline{\Omega}$ with $\sigma_n^{\mathrm{p}}(\boldsymbol{x}) \leqslant \sigma_0 < 0$, for all $\boldsymbol{x} \in \Gamma$. For $|\sigma_0|$ large enough we can suppose that during the seismic event (i.e. for $t \in [0, T]$) we have

$$\sigma_n(\boldsymbol{u}(t))(\boldsymbol{x}) + \sigma_n^{\mathrm{p}}(\boldsymbol{x}) \leqslant 0, \quad \text{for all } \boldsymbol{x} \in \Gamma, \tag{7}$$

which assures that no separation occurs on the fault Γ. The friction force also depends on the total slip

$$s(t) =: \int_0^t |[\dot{\boldsymbol{u}}_t(\xi)]|\,\mathrm{d}\xi$$

through a friction coefficient $\mu = \mu(s)$. Note that the total slip s is a non-reversible parameter and expresses the isotropic weakness of the friction resistance during the slip process. The anisotropic dependence of the friction law is beyond the scope of this paper. Concerning the regularity of $\mu : \Gamma \times \mathbb{R}_+ \to \mathbb{R}_+$ we suppose that the friction coefficient is a decreasing Lipschitz function, with respect to the slip. The equations (6) assert that the tangential (frictional) stress $\boldsymbol{\sigma}_t(\boldsymbol{u}(t)) + \boldsymbol{\sigma}_t^{\mathrm{p}}$ is bounded by the normal stress $\sigma_n(\boldsymbol{u}(t)) + \sigma_n^{\mathrm{p}}$ multiplied by the value of the friction coefficient μ. If such a limit is not attained sliding does not occur. Otherwise the friction stress is opposed to the slip rate $[\dot{\boldsymbol{u}}_t(t)]$ and its absolute value depends on the total slip $s(t)$ through μ.

Adding to the above equations and boundary conditions some initial conditions

$$\boldsymbol{u}(0) = \boldsymbol{u}_0, \quad \dot{\boldsymbol{u}}(0) = \boldsymbol{u}_1, \tag{8}$$

which are small perturbations of the equilibrium $\boldsymbol{u} = 0$, we can state the complete dynamic problem (1)–(8).

We shall use the following spaces of functions $\mathbf{H} =: L^2(\Omega)^d$, $\Sigma =: H^{-\frac{1}{2}}(\Gamma)$ (i.e. Σ is the dual of $H^{\frac{1}{2}}(\Gamma)$) and

$$\begin{aligned} \mathbf{V} &=: \{\boldsymbol{v} \in H^1(\Omega)^d; \boldsymbol{v} = 0 \text{ on } \Gamma_D, [v_n] = 0 \text{ on } \Gamma\}, \\ \mathbf{W} &=: \{\boldsymbol{v} \in H^1(\Omega)^d; \boldsymbol{v} = 0 \text{ on } \Gamma_D, [\boldsymbol{v}_t] = 0 \text{ on } \Gamma\}, \end{aligned} \tag{9}$$

and we consider the following bilinear applications

$$a(\boldsymbol{u}, \boldsymbol{v}) =: \int_\Omega (\mathcal{C}\boldsymbol{\varepsilon}(\boldsymbol{u})) : \boldsymbol{\varepsilon}(\boldsymbol{v})\,\mathrm{d}\Omega, \quad b(\boldsymbol{u}, \boldsymbol{v}) =: \int_\Omega \rho\boldsymbol{u}\cdot\boldsymbol{v}\,\mathrm{d}\Omega.$$

The variational formulation of the problem consists in finding $\boldsymbol{u}(t) \in \mathbf{V}$ with $\dot{\boldsymbol{u}}(t) \in \mathbf{V}, \ddot{\boldsymbol{u}}(t) \in \mathbf{H}$ and $\sigma_n(t) \in \Sigma$ verifying:

$$\begin{aligned} &b(\ddot{\boldsymbol{u}}(t), \boldsymbol{v} - \dot{\boldsymbol{u}}(t)) + a(\boldsymbol{u}(t), \boldsymbol{v} - \dot{\boldsymbol{u}}(t)) - \int_\Gamma \mu(s(t))(\sigma_n(t) + \sigma_n^{\mathrm{p}})(|[\boldsymbol{v}_t]| - |[\dot{\boldsymbol{u}}_t(t)]|) \\ &\quad + \int_\Gamma \boldsymbol{\sigma}_t^{\mathrm{p}} \cdot [\boldsymbol{v}_t - \dot{\boldsymbol{u}}_t(t)] \geqslant 0, \quad \forall \boldsymbol{v} \in \mathbf{V}, \end{aligned} \tag{10}$$

$$\int_\Gamma \sigma_n(t)[w_n] = b(\ddot{\boldsymbol{u}}(t), \boldsymbol{w}) + a(\boldsymbol{u}(t), \boldsymbol{w}), \quad \forall \boldsymbol{w} \in \mathbf{W}. \tag{11}$$

If $\sigma_n(t)$ is not regular enough, then the integral term on Γ is replaced by the duality product.

The above formulation is valid when the geometry of the fault is smooth. If the normal vector has discontinuities along the fault, the normal stress σ_n of the mixed finite element formulation, given through (11), is still well defined. This is a consequence of the facts that we deal in (11) with an integral formulation and the normal vector is well defined on each segment of the contact boundary. By contrast, the tangential slip rate $\dot{\boldsymbol{u}}_t$ is not well defined and the friction law (6) has to be reconsidered in the context of a discontinuity of the normal (see for instance [26]).

3. Time discretization

Explicit time-stepping schemes require a step value smaller than the critical CFL time step which is of the order of the ratio of the mesh size to the wave velocity. The duration of the initiation phase may be very large [10,14,29] and it may be very different from this threshold, so that the time step would be too small to allow simulations of the initiation phase. For this reason, we need an implicit time-stepping scheme allowing much larger values than the critical CFL time step.

The dynamic problem on Ω is discretized in time by the Newmark method with parameters $\beta = 1/4$ and $\gamma = 1/2$ (see for instance [23]). To this end, let $\Delta t > 0$ be the time step, N the maximum number of steps, and $T = N\Delta t$. We denote by $\boldsymbol{u}^k, \dot{\boldsymbol{u}}^k, \ddot{\boldsymbol{u}}^k$ and σ_n^k the discrete counterparts of the solution at time $t = k\Delta t$, i.e. $\boldsymbol{u}^k \approx \boldsymbol{u}(k\Delta t), \dot{\boldsymbol{u}}^k \approx \dot{\boldsymbol{u}}(k\Delta t), \ddot{\boldsymbol{u}}^k \approx \ddot{\boldsymbol{u}}(k\Delta t)$ and $\sigma_n^k \approx \sigma_n(k\Delta t)$ for all $0 \leqslant k \leqslant N$. The initial conditions (8) become

$$\boldsymbol{u}^0 = \boldsymbol{u}_0, \quad \dot{\boldsymbol{u}}^0 = \boldsymbol{u}_1, \quad \ddot{\boldsymbol{u}}^0 = \rho^{-1}\mathrm{div}(\boldsymbol{\sigma}(\boldsymbol{u}_0))$$

which is the starting point of a recursive problem. Suppose that we have constructed the solution up to $t = k\Delta t$, i.e. we have $\boldsymbol{u}^j, \dot{\boldsymbol{u}}^j, \ddot{\boldsymbol{u}}^j$ and σ_n^j for all $j \leqslant k$. In the Newmark method, the numerical solution $\boldsymbol{u}^{k+1}, \dot{\boldsymbol{u}}^{k+1}, \ddot{\boldsymbol{u}}^{k+1}$ and σ_n^{k+1} of (10) and (11) at $t = (k+1)\Delta t$ is obtained from

$$\boldsymbol{u}^{k+1} = \boldsymbol{u}^k + \Delta t\dot{\boldsymbol{u}}^k + \left(\frac{\Delta t}{2}\right)^2(\ddot{\boldsymbol{u}}^{k+1} + \ddot{\boldsymbol{u}}^k), \quad \dot{\boldsymbol{u}}^{k+1} = \dot{\boldsymbol{u}}^k + \frac{\Delta t}{2}(\ddot{\boldsymbol{u}}^{k+1} + \ddot{\boldsymbol{u}}^k)\dot{\boldsymbol{u}}^{k+1} \in \mathbf{V},$$

$$b(\ddot{\boldsymbol{u}}^{k+1}, \boldsymbol{v} - \dot{\boldsymbol{u}}^{k+1}) + a(\boldsymbol{u}^{k+1}, \boldsymbol{v} - \dot{\boldsymbol{u}}^{k+1}) - \int_\Gamma \mu(s^{k+1})(\sigma_n^{k+1} + \sigma_n^{\mathrm{p}})(|[\boldsymbol{v}_t]| - |[\dot{\boldsymbol{u}}_t^{k+1}]|) + \int_\Gamma \boldsymbol{\sigma}_t^{\mathrm{p}} \cdot [\boldsymbol{v}_t - \dot{\boldsymbol{u}}_t^{k+1}] \geqslant 0, \quad \forall \boldsymbol{v} \in \mathbf{V}$$

$$\sigma_n^{k+1} \in \Sigma, \quad \int_\Gamma \sigma_n^{k+1}[w_n] = b(\ddot{\boldsymbol{u}}^{k+1}, \boldsymbol{w}) + a(\boldsymbol{u}^{k+1}, \boldsymbol{w}), \quad \forall \boldsymbol{w} \in \mathbf{W},$$

where $\mathbf{V}$ and $\mathbf{W}$ are the spaces defined in (9) and s^{k+1} is the total slip

$$s^{k+1} = s^k + \frac{\Delta t}{2}(|[\dot{\boldsymbol{u}}_t^{k+1}]| + |[\dot{\boldsymbol{u}}_t^k]|).$$

By writing each term as a function of the velocity, the above problem becomes the following variational inequality:

Find $\dot{\boldsymbol{u}}^{k+1} \in \mathbf{V}$ and $\sigma_n^{k+1} \in \Sigma$ such that

$$b(\dot{\boldsymbol{u}}^{k+1}, \boldsymbol{v} - \dot{\boldsymbol{u}}^{k+1}) + \left(\frac{\Delta t}{2}\right)^2 a(\dot{\boldsymbol{u}}^{k+1}, \boldsymbol{v} - \dot{\boldsymbol{u}}^{k+1}) - \frac{\Delta t}{2}\int_\Gamma \mu_k(|[\dot{\boldsymbol{u}}_t^{k+1}]|)(\sigma_n^{k+1} + \sigma_n^{\mathrm{p}})(|[\boldsymbol{v}_t]| - |[\dot{\boldsymbol{u}}_t^{k+1}]|) \geqslant F_k(\boldsymbol{v} - \dot{\boldsymbol{u}}^{k+1}), \quad \forall \boldsymbol{v} \in \mathbf{V} \tag{12}$$

$$\frac{\Delta t}{2}\int_\Gamma \sigma_n^{k+1}[w_n] = b(\dot{\boldsymbol{u}}^{k+1}, \boldsymbol{w}) + \left(\frac{\Delta t}{2}\right)^2 a(\dot{\boldsymbol{u}}^{k+1}, w) - F_k(\boldsymbol{w}), \quad \forall \boldsymbol{w} \in \mathbf{W}, \tag{13}$$

where μ_k and F_k are given by

$$\mu_k(\alpha) = \mu\left(s^k + \frac{\Delta t}{2}(|[\dot{\boldsymbol{u}}_t^k]| + \alpha)\right), \quad \alpha \geqslant 0 \tag{14a}$$

$$F_k(\boldsymbol{v}) = b\left(\dot{\boldsymbol{u}}^k + \frac{\Delta t}{2}\ddot{\boldsymbol{u}}^k, \boldsymbol{v}\right) - \frac{\Delta t}{2}a\left(\boldsymbol{u}^k + \frac{\Delta t}{2}\dot{\boldsymbol{u}}^k, \boldsymbol{v}\right) - \frac{\Delta t}{2}\int_\Gamma \boldsymbol{\sigma}_t^{\mathrm{p}} \cdot [\boldsymbol{v}_t]. \tag{14b}$$

If $\dot{\boldsymbol{u}}^{k+1}$ is found, then one can deduce $\boldsymbol{u}^{k+1}$ and $\ddot{\boldsymbol{u}}^{k+1}$ through

$$\boldsymbol{u}^{k+1} = \boldsymbol{u}^k + \frac{\Delta t}{2}(\dot{\boldsymbol{u}}^k + \dot{\boldsymbol{u}}^{k+1}), \quad \ddot{\boldsymbol{u}}^{k+1} = 2\frac{\dot{\boldsymbol{u}}^{k+1} - \dot{\boldsymbol{u}}^k}{\Delta t} - \ddot{\boldsymbol{u}}^k. \tag{15}$$

Hence, the use of an implicit scheme for the wave equation with frictional type conditions on the faults will imply the resolution of a nonlinear problem, given by a variational inequality, at each time step.

4. Schwarz domain decomposition method

Although the following domain decomposition method is similar to that given in [6], for the convenience of the reader, we give below a short description of it. We consider over the domain Ω a conforming triangular mesh $\mathcal{T}_h$, of size h, such that the nodes on the sides of the fault Γ can be associated two by two having the same coordinates (one of them being located on the positive side of Γ and the other one on the negative side). In the following, we shall denote by $\boldsymbol{x}_i,\ i = 1,\ldots,n_d$ the interior nodes of $\mathcal{T}_h$ in Ω, and by $\boldsymbol{x}_i^+$ and $\boldsymbol{x}_i^-,\ i = 1,\ldots,n_f$, the pairs of nodes on the two sides of Γ having the same coordinates. We use the linear finite element spaces, and the shape functions in the nodal basis associated to $\mathcal{T}_h$ will be denoted by $\phi_i,\ i = 1,\ldots,n_d$, and ϕ_i^+ and $\phi_i^-,\ i = 1,\ldots,n_f$. Consequently, these basis functions will be piecewise linear, continuous functions such that: $\phi_i(\boldsymbol{x}_i) = 1$ and $\phi_i = 0$ at the other mesh nodes of $\mathcal{T}_h$, $\phi_i^+(\boldsymbol{x}_i^+) = 1$ and $\phi_i^+ = 0$ at the other mesh nodes of $\mathcal{T}_h$, and, finally, $\phi_i^-(\boldsymbol{x}_i^-) = 1$ and $\phi_i^- = 0$ at the other mesh nodes of $\mathcal{T}_h$.

We shall use a decomposition of the domain Ω made up of two overlapping subdomains, Ω_1 and Ω_2. The subdomain Ω_1 contains all the inner nodes of the domain $\Omega, \boldsymbol{x}_i,\ i = 1,\ldots,n_d$, whereas the nodes $\boldsymbol{x}_i^+$ and $\boldsymbol{x}_i^-,\ i = 1,\ldots,n_f$, lie in the subdomain Ω_2. First, we introduce other subdomains, denoted O_i. We write $O_1 = \Omega$, and for each pair of nodes $\boldsymbol{x}_i^+$ and $\boldsymbol{x}_i^-$ on Γ, we define the subdomains $O_{i+1},\ i = 1,\ldots,n_f$, which are obtained by the union of the triangles (in the 2D case) or tetrahedra (in the 3D case) which have a vertex at either node $\boldsymbol{x}_i^+$ or $\boldsymbol{x}_i^-$ on Γ (see Fig. 1). Consequently, $O_{i+1} = \mathrm{Int}(\mathrm{supp}\,\phi_i^+) \cup \mathrm{Int}(\mathrm{supp}\,\phi_i^-),\ i = 1,\ldots,n_f$. Now, we write $\Omega_1 = O_1$, and the second subdomain will be defined as $\Omega_2 = \bigcup_{i=1}^{n_f} O_{i+1}$.

Roughly speaking, the Schwarz algorithm is an iterative procedure such that, within an iteration, similar problems are solved in each subdomain. The unknowns of each subproblem are the unknowns of the initial problem corresponding to the nodes of the subdomain. The boundary conditions are of Dirichlet type: on the boundary of each subdomain, the values of the solutions of the other subdomains are imposed. By the above decomposition of the domain Ω, the unknowns inside the domain and those on Γ lie in different subdomains. Moreover, since the domain Ω_1 has no unknown on the fault, the subproblem on Ω_1 becomes linear, i.e. it reduces to solving an algebraic linear system. The nonlinear subproblem on Ω_2 is solved by the same Schwarz algorithm by using $O_2,\ldots,O_M, M = n_f + 1$, as a domain decomposition of Ω_2. Consequently, at each global iteration of the algorithm, we (sub-)iterate over $O_2,\ldots,O_M$ until the convergence over whole Ω_2 is achieved, and then we solve the algebraic linear system corresponding to Ω_1. The nonlinear subproblems over each $O_2,\ldots,O_M$ are of a small size (they have three unknowns in 2D and five unknowns in 3D) and it allows us to use efficient solvers which will be given in Section 5.

To introduce the finite element form on Ω of problem (12) and (13), first we define the space

$$\mathbf{U}^h =: \{\boldsymbol{v} \in C^0(\Omega)^d : \boldsymbol{v}_{|\tau} \in P_1(\tau), \tau \in \mathcal{T}_h, \boldsymbol{v} = 0 \text{ on } \Gamma_D\}.$$

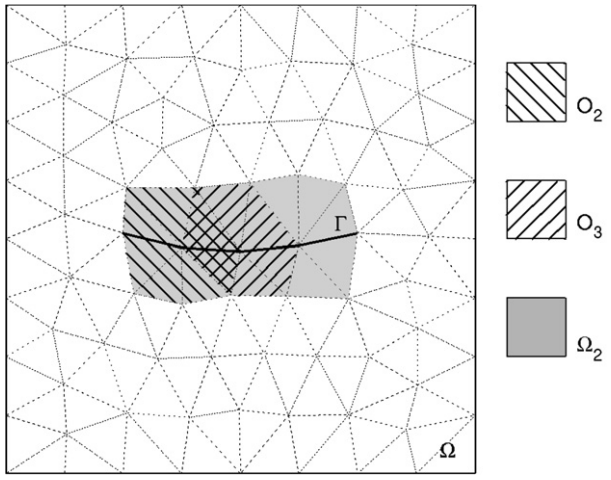

Fig. 1. Decomposition of Ω. The subdomain Ω_2 has been shaded, and the first two small subdomains O_2 and O_3 are pointed out by means of hachures.

Here, we assume that the boundary Γ is composed of polygonal curves (in 2D) or triangular polyhedral surfaces (in 3D), without any additional branch (that is, in 2D, each point of the discretized interface Γ is connected to two other fault points at most). Then, for each pair of nodes $\boldsymbol{x}_i^+$ and $\boldsymbol{x}_i^-$ on Γ, we define the normal unit vector $\boldsymbol{n}_i$ as the directing vector of the bisectrix of the (polyhedral) angle associated to the common geometrical point of x_i^+ and x_i^-, and with direction from $\boldsymbol{x}_i^+$ to $\boldsymbol{x}_i^-$. Now, denoting by φ_i the common trace of ϕ_i^+ and ϕ_i^- on Γ, for any $\boldsymbol{v} \in \mathbf{U}^h$, we write

$$[v_n] = \sum_{i=1}^{n_f} \{\boldsymbol{v}(\boldsymbol{x}_i^+) - \boldsymbol{v}(\boldsymbol{x}_i^-)\} \cdot \boldsymbol{n}_i \varphi_i,$$

$$[\boldsymbol{v}_t] = \sum_{i=1}^{n_f} \{\boldsymbol{v}(\boldsymbol{x}_i^+) - \boldsymbol{v}(\boldsymbol{x}_i^-) - [v_n]\boldsymbol{n}_i\} \varphi_i.$$

Using these definitions, we associate to the spaces introduced in (9) the linear finite element spaces

$$\mathbf{V}^h =: \{\boldsymbol{v} \in \mathbf{U}^h : [v_n] = 0 \text{ on } \Gamma\},$$

$$\mathbf{W}^h =: \{\boldsymbol{v} \in \mathbf{U}^h : [\boldsymbol{v}_t] = 0 \text{ on } \Gamma\}.$$

Also, we have to associate to the space Σ of the normal stresses on Γ, σ_n, a space of Lagrange multipliers, which we shall denote Σ^h. In the two-dimensional case we shall use the space introduced in [45] which is generated by some nodal basis functions $\psi_i,\ i = 1, \ldots, n_f$, having the orthogonality property

$$\int_\Gamma \varphi_i \psi_j = \delta_{ij} \int_\Gamma \varphi_i. \tag{16}$$

Now we write the finite element problem associated to (12) and (13) for a fixed time step $k+1$ as: find $\dot{\boldsymbol{u}} \in \mathbf{V}^h$ and $\sigma_n \in \Sigma^h$ such that

$$b(\dot{\boldsymbol{u}}, \boldsymbol{v} - \dot{\boldsymbol{u}}) + \left(\frac{\Delta t}{2}\right)^2 a(\dot{\boldsymbol{u}}, \boldsymbol{v} - \dot{\boldsymbol{u}})$$

$$- \sum_{i=1}^{n_f} \frac{\Delta t}{2} \int_\Gamma \mu_k(|[\dot{\boldsymbol{u}}_t]_i|)(\sigma_n + \sigma_n^{\mathrm{p}})(|[\boldsymbol{v}_t]_i| - |[\dot{\boldsymbol{u}}_t]_i|)\varphi_i \geqslant F_k(\boldsymbol{v} - \dot{\boldsymbol{u}}), \quad \forall \boldsymbol{v} \in \mathbf{V}^h, \tag{17}$$

$$\frac{\Delta t}{2} \int_\Gamma \sigma_n [w_n] = b(\dot{\boldsymbol{u}}, \boldsymbol{w}) + \left(\frac{\Delta t}{2}\right)^2 a(\dot{\boldsymbol{u}}, w) - F_k(\boldsymbol{w}), \quad \forall \boldsymbol{w} \in \mathbf{W}^h, \tag{18}$$

where μ_k and F_k follow ((14). Note that we have dropped the index $k+1$ denoting the time step, and the integral over Γ has been approximated as

$$\int_\Gamma \mu_k(|[\dot{\boldsymbol{u}}_t]|)(\sigma_n + \sigma_n^{\mathrm{p}})(|[\boldsymbol{v}_t]| - |[\dot{\boldsymbol{u}}_t]|) = \sum_{i=1}^{n_f} \int_\Gamma \mu_{ki}(|[\dot{\boldsymbol{u}}_t]_i|)(\sigma_n + \sigma_n^{\mathrm{p}})(|[\boldsymbol{v}_t]_i| - |[\dot{\boldsymbol{u}}_t]_i|)\varphi_i$$

with $[\boldsymbol{v}_t]_i = \boldsymbol{v}_t(\boldsymbol{x}_i^+) - \boldsymbol{v}_t(\boldsymbol{x}_i^-)$ and

$$\mu_{ki}(\alpha) = \mu\left(\boldsymbol{z}_i, s_i^k + \frac{\Delta t}{2}(|[\dot{\boldsymbol{u}}_t^k]_i| + \alpha)\right), \quad \alpha \geqslant 0,\ s_i^k =: \int_0^{k\Delta t} |[\dot{\boldsymbol{u}}_t]_i|, \tag{19}$$

$\boldsymbol{z}_i$ being the common geometrical point of x_i^+ and x_i^- (as μ can be a function of the position on Γ, too). To explicitly write the Schwarz algorithm corresponding to the decomposition of Ω by the subdomains Ω_1 and Ω_2, we have to introduce the functional subspaces associated with this decomposition. Hence, we associate to Ω_1 the space

$$\mathbf{U}_1^h =: \{\boldsymbol{v} \in \mathbf{U}^h : v = 0 \text{ on } \Gamma\},$$

and to Ω_2 the space

$$\mathbf{U}_2^h =: \{\boldsymbol{v} \in \mathbf{U}^h : v = 0 \text{ in } \Omega \setminus \Omega_2\}.$$

Note that in fact, since $\Omega_1 = \Omega$, the method operates rather as a space decomposition than as a domain decomposition. Since the solution in $\mathbf{U}_2^h$ is obtained by the same iterative method, we also introduce the spaces corresponding to the subdomains $O_{i+1}, i = 1, \ldots, n_f$, as

$$\mathbf{U}_{2i}^h =: \{\boldsymbol{v} \in \mathbf{U}^h : v = 0 \text{ in } \Omega \setminus O_{i+1}\}.$$

Also, we define similar subspaces $\mathbf{V}_1^h, \mathbf{V}_2^h, \mathbf{V}_{2i}^h$ and $\mathbf{W}_1^h, \mathbf{W}_2^h, \mathbf{W}_{2i}^h$. Now, we can propose an iterative algorithm to solve problem (17) and (18).

Algorithm. The algorithm starts with an arbitrary $\dot{\boldsymbol{u}}^0 = \dot{\boldsymbol{u}}_1^0 + \dot{\boldsymbol{u}}_2^0, \dot{\boldsymbol{u}}_1^0 \in \mathbf{V}_1^h, \dot{\boldsymbol{u}}_2^0 = \dot{\boldsymbol{u}}_{21}^0 + \cdots + \dot{\boldsymbol{u}}_{2n_f}^0 \in \mathbf{V}_2^h, \dot{\boldsymbol{u}}_{2i}^0 \in \mathbf{V}_{2i}^h$, $i = 1, \ldots, n_f$. We assume that after n iterations we have obtained $\dot{\boldsymbol{u}}^n = \dot{\boldsymbol{u}}_1^n + \dot{\boldsymbol{u}}_2^n, \dot{\boldsymbol{u}}_1^n \in \mathbf{V}_1^h, \dot{\boldsymbol{u}}_2^n = \dot{\boldsymbol{u}}_{21}^n + \cdots + \dot{\boldsymbol{u}}_{2n_f}^n \in \mathbf{V}_2^h, \dot{\boldsymbol{u}}_{2i}^n \in \mathbf{V}_{2i}^h, i = 1, \ldots, n_f$.

First step. We compute $\dot{\boldsymbol{u}}_1^{n+1} \in \mathbf{V}_1^h$, the approximation of $\dot{\boldsymbol{u}}$ on Ω_1 at iteration $n+1$, as the solution of the algebraic linear system

$$b(\dot{\boldsymbol{u}}_1^{n+1} + \dot{\boldsymbol{u}}_2^n, \boldsymbol{v}) + \left(\frac{\Delta t}{2}\right)^2 a(\dot{\boldsymbol{u}}_1^{n+1} + \dot{\boldsymbol{u}}_2^n, \boldsymbol{v}) = F_k(\boldsymbol{v}) \quad \text{for all } \boldsymbol{v} \in \mathbf{V}_1^h. \tag{20}$$

Second step. We iteratively compute $\dot{\boldsymbol{u}}_2^{n+1} \in \mathbf{V}_2^h$, the approximation of $\dot{\boldsymbol{u}}$ on Ω_2, by iterating over the subspaces $\mathbf{V}_{21}^h, \ldots, \mathbf{V}_{2n_f}^h$. Let us write $\dot{\boldsymbol{u}}_2^{n+1,0} = \dot{\boldsymbol{u}}_2^n$ and $\dot{\boldsymbol{u}}_{2i}^{n+1,0} = \dot{\boldsymbol{u}}_{2i}^n, i = 1, \ldots, n_f$. The approximation $\dot{\boldsymbol{u}}_{2i}^{n+1,m+1} \in \mathbf{V}_{2i}^h$ of $\dot{\boldsymbol{u}}$ (at the overall iteration $n+1$ and the local iteration $m+1$ over the subspaces of $\mathbf{V}_2^h$) is the solution of the following *local nonlinear problem* (LNP):

$$\begin{aligned} &b(\tilde{\dot{\boldsymbol{u}}}_{2i}^{n+1,m+1}, \boldsymbol{v}_{2i} - \dot{\boldsymbol{u}}_{2i}^{n+1,m+1}) + \left(\frac{\Delta t}{2}\right)^2 a(\tilde{\dot{\boldsymbol{u}}}_{2i}^{n+1,m+1}, \boldsymbol{v}_{2i} - \dot{\boldsymbol{u}}_{2i}^{n+1,m+1}) \\ &\quad - \frac{\Delta t}{2}\int_\Gamma \mu_{ki}(|[(\dot{\boldsymbol{u}}_{2i}^{n+1,m+1})_t]|)(\sigma_n + \sigma_n^{\mathrm{p}})(|[(\boldsymbol{v}_{2i})_t]| - |[(\dot{\boldsymbol{u}}_{2i}^{n+1,m+1})_t]|)\varphi_i \geqslant F_k(\boldsymbol{v}_{2i} - \dot{\boldsymbol{u}}_{2i}^{n+1,m+1}), \quad \forall \boldsymbol{v}_{2i} \in \mathbf{V}_{2i}^h, \end{aligned} \tag{21}$$

$$\frac{\Delta t}{2}\int_\Gamma \sigma_n[(w_{2i})_n] = b(\tilde{\dot{\boldsymbol{u}}}_{2i}^{n+1,m+1}, \boldsymbol{w}_{2i}) + \left(\frac{\Delta t}{2}\right)^2 a(\tilde{\dot{\boldsymbol{u}}}_{2i}^{n+1,m+1}, \boldsymbol{w}_{2i}) - F_k(\boldsymbol{w}_{2i}), \quad \forall \boldsymbol{w}_{2i} \in \mathbf{W}_{2i}^h. \tag{22}$$

In the above equations we have denoted

$$\tilde{\dot{\boldsymbol{u}}}_{2i}^{n+1,m+1} = \dot{\boldsymbol{u}}_1^{n+1} + \sum_{j=1}^{i} \dot{\boldsymbol{u}}_{2j}^{n+1,m+1} + \sum_{j=i+1}^{n_f} \dot{\boldsymbol{u}}_{2j}^{n+1,m}. \tag{23}$$

Finally, assuming that the convergence of iterative process (21) and (22) is achieved after m_{end} iterations, we write

$$\dot{\boldsymbol{u}}_{2i}^{n+1} = \dot{\boldsymbol{u}}_{2i}^{n+1,m_{\mathrm{end}}}, \quad i = 1, \ldots, n_f,$$

and proceed to iteration $n+2$ of the global iterative process (20)–(22).

5. Solution of local nonlinear problems

In this section we focus on the resolution of (LNP), i.e. the local nonlinear problem (21) and (22). For the sake of simplicity, we apply the above algorithm to a 2D problem (i.e. $d = 2$). Evidently, the linear algebraic system (20) has a unique solution. Again, since nonlinear problem (21) and (22) contains only three unknowns, we can solve it almost explicitly. We give here a detailed algorithm to solve this problem and show the existence and the uniqueness of its solution if the value of Δt is small enough. Note that the following calculations concern slip-weakening friction, but the method also works if the friction increases with slip (slip-strengthening case), or if the rate-and-state friction law is used.

First, we write the local unknowns $\boldsymbol{v}_i^+, \boldsymbol{v}_i^-$ in terms of mean values and jumps in both normal and tangential directions, denoted by $\eta_{v_i}^n, \delta_{v_i}^n, \eta_{v_i}^t, \delta_{v_i}^t \in \mathbb{R}$. For a given $i = 1, \ldots, n_f$, any $\boldsymbol{v}_{2i} \in \mathbf{U}_{2i}^h$ can be written as a vector function of four components,

$$\boldsymbol{v}_{2i} = \boldsymbol{v}_i^+ \phi_i^+ + \boldsymbol{v}_i^- \phi_i^-,$$

where $\boldsymbol{v}_i^+$ and $\boldsymbol{v}_i^-$ are two-dimensional vectors which can be written as

$$\boldsymbol{v}_i^+ = \frac{1}{2}(\eta_{v_i}^n + \delta_{v_i}^n)\boldsymbol{n}_i + \frac{1}{2}(\eta_{v_i}^t + \delta_{v_i}^t)\boldsymbol{t}_i,$$
$$\boldsymbol{v}_i^- = \frac{1}{2}(\eta_{v_i}^n - \delta_{v_i}^n)\boldsymbol{n}_i + \frac{1}{2}(\eta_{v_i}^t - \delta_{v_i}^t)\boldsymbol{t}_i,$$

where $\boldsymbol{t}_i$ is the unit tangent vector defined at the common geometrical point of x_i^+ and x_i^-. If $\boldsymbol{v}_{2i} \in \mathbf{V}_{2i}^h$ then $\delta_{v_i}^n = 0$, and if $\boldsymbol{w}_{2i} \in \mathbf{W}_{2i}^h$ then $\delta_{w_i}^t = 0$.

With these notations, since $\delta_{\dot{\boldsymbol{u}}_{2i}^{n+1,m+1}}^n = 0$, the unknowns of problem (21) and (22) are

$$r := \eta_{\dot{\boldsymbol{u}}_{2i}^{n+1,m+1}}^n, \quad s := \eta_{\dot{\boldsymbol{u}}_{2i}^{n+1,m+1}}^t, \quad t := \delta_{\dot{\boldsymbol{u}}_{2i}^{n+1,m+1}}^t.$$

Evidently, variables r, s and t depend on iterations $n+1$ and $m+1$, and on the geometrical point i, but for simplicity we have dropped the indices. Formula (23) reads now

$$\tilde{\dot{\boldsymbol{u}}}_{2i}^{n+1,m+1} = \left\{\frac{1}{2}r\boldsymbol{n}_i + \frac{1}{2}(s+t)\boldsymbol{t}_i\right\}\phi_i^+ + \left\{\frac{1}{2}r\boldsymbol{n}_i + \frac{1}{2}(s-t)\boldsymbol{t}_i\right\}\phi_i^- + \hat{\dot{\boldsymbol{u}}}_{2i}^{n+1,m+1}, \tag{24}$$

where

$$\hat{\dot{\boldsymbol{u}}}_{2i}^{n+1,m+1} := \dot{\boldsymbol{u}}_1^{n+1} + \dot{\boldsymbol{u}}_{21}^{n+1,m+1} + \cdots + \dot{\boldsymbol{u}}_{2(i-1)}^{n+1,m+1} + \dot{\boldsymbol{u}}_{2(i+1)}^{n+1,m} + \cdots + \dot{\boldsymbol{u}}_{2n_f}^{n+1,m}$$

is known. We write in the following a problem composed of two equations and one inequality, which unknowns are r, s and t, and which is equivalent to (21) and (22).

First, the following two equations on the variables r, s and t are deduced from (21) (see the Appendix for details)

$$a_{nn}^+ r + b_{nt}^+ s + b_{nt}^- t = d_n^+, \tag{25}$$
$$b_{nt}^+ r + a_{tt}^+ s + a_{tt}^- t = d_t^+, \tag{26}$$

where the coefficients are real constants which can be computed at each iteration $m+1$.

Also, as it follows from the Appendix, the nonlinear frictional boundary condition can be written as

$$(b_{nt}^- r + a_{tt}^- s + a_{tt}^+ t - d_t^-)(\bar{t} - t) - \left(a_{nn}^- r + b_{nt}^- s + b_{nt}^+ t - d_n^- + (\sigma^{\mathrm{p}})_n^i \Delta t \int_\Gamma \varphi_i\right)\mu_{ki}(|t|)(|\bar{t}| - |t|) \geqslant 0, \quad \forall \bar{t} \in \mathbb{R}. \tag{27}$$

Here, variables $(\sigma^{\mathrm{p}})_n^i$ are given by

$$\sigma_n^{\mathrm{p}} = \sum_{i=1}^{n_f} (\sigma^{\mathrm{p}})_n^i \psi_i,$$

where $\psi_i,\ i = 1, \ldots, n_f$, are the Lagrange multipliers with property (16).

In order to write the inequality (27) on a single variable, t, we solve the algebraic system given by (25) and (26), finding r and s as functions of t,

$$r = -\frac{D_{rt}}{D}t + \frac{D_r}{D}, \quad s = -\frac{D_{st}}{D}t + \frac{D_s}{D}, \tag{28}$$

where

$$D = a_{nn}^+ a_{tt}^+ - (b_{nt}^+)^2, \quad D_{rt} = b_{nt}^- a_{tt}^+ - b_{nt}^+ a_{tt}^-, \quad D_{st} = a_{nn}^+ a_{tt}^- - b_{nt}^+ b_{nt}^-, \quad D_r = d_n^+ a_{tt}^+ - d_t^+ b_{nt}^+, \quad D_s = d_t^+ a_{nn}^+ - d_n^+ b_{nt}^+. \tag{29}$$

Replacing in the above expression of D the expressions of a_{nn}^+, a_{tt}^+ and b_{nt}^+ in (42) and (43), derived in the Appendix, we get that $D > 0$ for any $\Delta t > 0$. Consequently, r and s are correctly defined in (28) for any value of $\Delta t > 0$. Replacing in (27) the expressions of r and s in (28), we get the inequality

$$(at+b)(\bar{t}-t)+\mu_{ki}(|t|)(ct+d)(|\bar{t}|-|t|)\geqslant 0,\quad \forall \bar{t}\in\mathbb{R}, \tag{30}$$

where

$$a=-D_{rt}b_{nt}^{-}-D_{st}a_{tt}^{-}+Da_{tt}^{+},\quad b=D_rb_{nt}^{-}+D_sa_{tt}^{-}-Dd_t^{-},\quad c=D_{rt}a_{nn}^{-}+D_{st}b_{nt}^{-}-Db_{nt}^{+},$$
$$d=-D_ra_{nn}^{-}-D_sb_{nt}^{-}+Dd_n^{-}-D(\sigma^{\mathrm{p}})_n^i\Delta t\int_\Gamma\varphi_i. \tag{31}$$

We see that $a\to\frac{1}{2}b(\boldsymbol{n}_i\phi_i^{+}+\boldsymbol{n}_i\phi_i^{-},\boldsymbol{n}_i\phi_i^{+}+\boldsymbol{n}_i\phi_i^{-})b(\boldsymbol{t}_i\phi_i^{+}+\boldsymbol{t}_i\phi_i^{-},\boldsymbol{t}_i\phi_i^{+}+\boldsymbol{t}_i\phi_i^{-})^2>0$ and $c\to 0$ as $\Delta t\to 0$, and consequently, for small enough Δt, we have

$$a-|c|\mu(0)>0. \tag{32}$$

Now we show that

The inequality (30) *has a unique solution for* Δt *small enough.* (33)

and we deduce an algorithm to solve (30).

As stated at the beginning of this paper, the friction coefficient is a decreasing non-negative Lipschitz function, with respect to the total slip. Consequently, using (19), we get that there exist $\mu_0\geqslant\mu_\infty\geqslant 0$ and $M>0$ such that

$$\mu_\infty\leqslant\mu_{ki}(\bar{t})\leqslant\mu_0\quad\text{for any }\bar{t}\geqslant 0$$
$$0\leqslant\mu_{ki}(\bar{t}_1)-\mu_{ki}(\bar{t}_2)\leqslant M\frac{\Delta t}{2}(\bar{t}_2-\bar{t}_1)\quad\text{for any }\bar{t}_2\geqslant\bar{t}_1\geqslant 0. \tag{34}$$

Now, taking in turn $\bar{t}=0$ and $\bar{t}=t$ in (30), we get that this inequality is equivalent to

$$t(at+b)+|t|\mu_{ki}(|t|)(ct+d)=0,\quad \mu_{ki}(|t|)(ct+d)\geqslant|at+b|. \tag{35}$$

Moreover, we see that if t satisfies (35) then we have

$$t=0\Longleftrightarrow\mu_{ki}(0)d\geqslant|b| \tag{36a}$$

$$t>0\Longleftrightarrow 0<t\leqslant-\frac{b}{a},\quad t=\frac{-b-d\mu_{ki}(t)}{a+c\mu_{ki}(t)}$$
$$\Longleftrightarrow\quad b+d\mu_{ki}(t)<0,\quad ad-bc\geqslant 0,\quad t=\frac{-b-d\mu_{ki}(t)}{a+c\mu_{ki}(t)} \tag{36b}$$

$$t<0\Longleftrightarrow\ -\frac{b}{a}\leqslant t<0,\quad t=\frac{-b+d\mu_{ki}(-t)}{a-c\mu_{ki}(-t)}$$
$$\Longleftrightarrow b-d\mu_{ki}(-t)>0,\quad ad-bc\geqslant 0,\quad t=\frac{-b+d\mu_{ki}(-t)}{a-c\mu_{ki}(-t)}. \tag{36c}$$

We have used (32) and (35) to write the equivalences in (36b) and (36c). In the following, we use (36) to establish the existence and the uniqueness of the solution of problem (30).

First, we notice that the condition $ad-bc\geqslant 0$ in (36b) and (36c) is equivalent to $ct+d\geqslant 0$, and, from (30) and (49), it is equivalent to $\sigma_n^i+(\sigma^{\mathrm{p}})_n^i\leqslant 0$, which is assumed to hold true in (7).

Now, we prove the uniqueness of the solution of problem (30). Since $a>0$, from (36b) and (36c), we get that if (30) has a positive solution then $b<0$, and if (30) has a negative solution then $b>0$. Consequently, we have:

Statement 1. Inequality (30) cannot have positive solutions and negative solutions at the same time.

From (34), we get

$$\left|\frac{-b-d\mu_{ki}(t_2)}{a+c\mu_{ki}(t_2)}-\frac{-b-d\mu_{ki}(t_1)}{a+c\mu_{ki}(t_1)}\right|\leqslant M\frac{\Delta t}{2}\frac{ad-bc}{(a-|c|\mu_{ki}(0))^2}|t_2-t_1|\quad\text{for } t_1,t_2\geqslant 0$$
$$\left|\frac{-b+d\mu_{ki}(-t_2)}{a-c\mu_{ki}(-t_2)}-\frac{-b+d\mu_{ki}(-t_1)}{a-c\mu_{ki}(-t_1)}\right|\leqslant M\frac{\Delta t}{2}\frac{ad-bc}{(a-|c|\mu_{ki}(0))^2}|t_2-t_1|\quad\text{for } t_1,t_2\leqslant 0 \tag{37}$$

and, using (36b) and (36c), we conclude:

Statement 2. For

$$\Delta t < \frac{2}{M}\frac{(a-|c|\mu_{ki}(0))^2}{ad-bc}, \tag{38}$$

inequality (30) cannot have more than one positive solution or more than one negative solution.

Now we assume that $\mu_{ki}(0)d \geqslant |b|$, i.e. $t=0$ is a solution of Eq. (30). Assuming that inequality (30) has another solution $t>0$, then $b<0$, hence $b+\mu_{ki}(0)d \geqslant 0$ and

$$\frac{-b-d\mu_{ki}(t)}{a+c\mu_{ki}(t)} - t = \frac{-b-d\mu_{ki}(0)}{a+c\mu_{ki}(0)} - \frac{ad-bc}{(a+c\mu_{ki}(0))(a+c\mu_{ki}(t))}(\mu_{ki}(t)-\mu_{ki}(0)) - t \leqslant M\frac{\Delta t}{2}\frac{ad-bc}{(a-|c|\mu_{ki}(0))^2}t - t.$$

Consequently, if Δt satisfies (38), then inequality (30) cannot have a positive solution. We can get a similar result for the negative solutions, and finally we can conclude:

Statement 3. If Δt satisfies (38), then inequality (30) cannot have the zero solution and another one different from zero at the same time.

The uniqueness of the solution of inequality (30) is deduced from the above Statements 1–3.

To prove the existence of the solution of inequality (30), we assume that $\mu_{ki}(0)d < |b|$, i.e. $t=0$ is not a solution of inequality (30). Since μ_{ki} is a decreasing function, we get that $\mu_{ki}(\bar{t})d \leqslant |b|$ for any $\bar{t} \geqslant 0$. If $b<0$, we have $b+\mu_{ki}(\bar{t})d \leqslant 0$, and using it and the fact that $ad-bc \geqslant 0$, we get that application $\bar{t} \mapsto \frac{-b-d\mu_{ki}(\bar{t})}{a+c\mu_{ki}(\bar{t})}$) maps the interval $[0,-\frac{b}{a}]$ into itself. Taking into account (37), it follows from the fix point theorem that inequality (30) has a unique positive solution. By a similar reasoning, we get that inequality (30) has a unique negative solution if $b>0$, and the statement (33) is proved.

Taking into account condition (38) and the values of Δt for which (32) holds, we can get an effective upper bound $\Delta t_{\max}$ such that inequality (30) has a unique solution for $0 \leqslant \Delta t \leqslant \Delta t_{\max}$. Note that this uniqueness condition, involving the time step value, depends on the friction weakening rate. The computation of $\Delta t_{\max}$ is not straightforward but, in all the numerical simulations we performed so far, we found that the uniqueness condition was fulfilled for time step values much larger than the CFL threshold (Courant condition for stability of explicit time stepping).

Assuming that $0 \leqslant \Delta t \leqslant \Delta t_{\max}$ and $\sigma_n + \sigma_n^{\mathrm{p}} \leqslant 0$ we propose in the following an algorithm for solving problem (21) and (22).

Algorithm

(1) We calculate a, b, c and d from (31) using (42), (43), (48), (50) and (29).

(2.1) If $\mu_{ki}(0)d \geqslant |b|$, then $t=0$ is the unique solution of inequality (30).

(2.2) If $\mu_{ki}(0)d < |b|$ and $b<0$, then inequality (30) has a unique solution $t>0$ which satisfies equation

$$t = \frac{-b-d\mu_{ki}(t)}{a+c\mu_{ki}(t)}.$$

(2.3) If $\mu_{ki}(0)d < |b|$ and $b>0$, then inequality (30) has a unique solution $t<0$ which satisfies equation

$$t = \frac{-b+d\mu_{ki}(-t)}{a-c\mu_{ki}(-t)}.$$

(3) We calculate r and s from (28).

(4) We write the solution of problem (21) and (22) as

$$\dot{\boldsymbol{u}}_{2i}^{n+1,m+1} = \left\{\frac{1}{2}r\boldsymbol{n}_i + \frac{1}{2}(s+t)\boldsymbol{t}_i\right\}\phi_i^+ + \left\{\frac{1}{2}r\boldsymbol{n}_i + \frac{1}{2}(s-t)\boldsymbol{t}_i\right\}\phi_i^-.$$

6. Numerical results

The numerical tests are presented below in three parts. The first two parts investigate the performance of the algorithm detailed in Section 4 to solve (17) and (18). To this end, two kinds of fault instabilities are

considered. In Section 6.1, the initiation phase of earthquakes is modeled by slip weakening friction, without any variation of normal stress. Conversely, in Section 6.2, the fault is perturbed by normal stress variations whereas the friction coefficient remains constant. Finally, in Section 6.3, a more complex and realistic simulation is performed where both types of instabilities are present. All these computations were performed on a 3 GHz Pentium 4 M630 computer.

In the following, we consider the in-plane configuration ($d = 2$), and we assume that the elastic material is isotropic and homogeneous:

$$\mathcal{C}_{ijkl}(x) = \lambda\delta_{ij}\delta_{kl} + 2G\delta_{ik}\delta_{jl}$$

with λ, G being the Lamé coefficients.

In Sections 6.1 and 6.2 the equations are written in a non-dimensional formulation, by setting all physical parameters (ρ, λ, G) equal to 1 and by considering Γ to be the straight fault $[-1, 1] \times \{0\}$. In the realistic application of Section 6.3, all these parameters will be chosen to fit typical seismological scaling.

6.1. Slip weakening with constant normal stress

We intend here to prove the ability of our numerical method in capturing the instabilities generated by friction weakening, resulting in exponentially growing slip amplitude (initiation phase). The conservation of the total energy is also addressed. These tests, which have been already conducted in the anti-plane case [6], are performed here in the in-plane configuration.

The computational domain $\overline{\Omega}$ is the square $[-5, 5] \times [-5, 5]$. The friction coefficient is supposed to be piecewise linear:

$$\mu(x, s) = \begin{cases} \mu_s(\boldsymbol{x}) - \frac{\mu_s(\boldsymbol{x}) - \mu_d(\boldsymbol{x})}{D_c(\boldsymbol{x})} s, & \text{if } s \leqslant D_c, \\ \mu_d(\boldsymbol{x}), & \text{if } s > D_c \end{cases} \tag{39}$$

with $\mu_s(\boldsymbol{x}) = 2.0$ and $\mu_d(\boldsymbol{x}) = 1.0$. The critical slip is $D_c(\boldsymbol{x}) = 0.75$. The (initial) pre-stress components on the fault are $\sigma_t^p = -2.0$ and $\sigma_n^p = -1.0$, verifying $\sigma_t^p = \mu_s \sigma_n^p$, so that the fault is at the failure level everywhere at the initial time. This assumption is not realistic: in general, only a small portion of the fault is at the failure level initially, and the propagation of waves from the expanding crack increases the stress elsewhere to the failure level. The choice of this initial state is motivated by two reasons. The first one is physical: we want to describe the unstable evolution of the slip near an equilibrium position. The second reason is technical: we want to point out the ability of the method in capturing instabilities during the initiation phase.

This initial unstable equilibrium position is perturbed by a small velocity impulse (i.e. $\boldsymbol{u}_0 \equiv 0, |\boldsymbol{u}_1| << 1$). The shape and location of the initial perturbation of the velocity field $\boldsymbol{u}_1$ has no influence on the behavior of the unstable solution. However, for computational reasons, we chose it as a continuous function on Ω which support $\{x \in \Omega; \boldsymbol{u}_1(x) \neq 0\}$ is small and located in the neighborhood of the fault system. More precisely, $\boldsymbol{u}_1$ exhibits a small jump on Γ with a gaussian-like shape of width α and amplitude A, centered in the middle of the fault and prolonged by two half-gaussians in the surrounding medium:

$$\boldsymbol{u}_0 \equiv 0, \quad \boldsymbol{u}_1(x_1, x_2) = \begin{cases} (\varphi_\alpha(x_1^2 + x_2^2), 0) & \text{if } x_2 \geqslant 0, \\ (-\varphi_\alpha(x_1^2 + x_2^2), 0) & \text{if } x_2 < 0 \end{cases} \tag{40}$$

with $\varphi_\alpha(z) = A \exp(z/(\alpha^2 - z))$ if $0 \leqslant z < \alpha^2$, and $\varphi_\alpha(z) = 0$ if $z \geqslant \alpha^2$. The amplitude and width are $A = 10^{-4}$ and $\alpha = 0.5$. With this choice of initial condition, which is antisymmetric with respect to x_2, the normal over-stress $\sigma_n(\boldsymbol{u})$ on Γ is expected to remain equal to zero.

First, in order to discriminate numerical errors due to the time-stepping scheme and finite element spatial discretization from errors due to the Schwarz algorithm, we analyzed on a single time step computation the influence of the spatial and temporal discretization parameters (mesh size h and time step Δt) on the solution accuracy. These tests, similar to those performed in the anti-plane case [6], led to similar results: convergence is achieved with respect to the mesh size, and the number of Schwarz iterations is an increasing, almost linear function of the time step. These results are not described in this paper; we refer to [6] for more details. Then, to investigate convergence on a time interval, we used a heterogeneous mesh (10,043 nodes, 80 edges on the

fault) to simulate the system evolution in the time period $[0, T]$ ($T = 5$ s) with several different values of the time step. The physical parameters in (39) are such that the characteristic pattern of the initiation phase (earthquake nucleation) is excited, but the calculation is stopped before the rupture phase begins. Moreover, each point on Γ is initially put at the failure level ($\sigma_t^p = \mu_s \sigma_n^p$). These tests are detailed in the following paragraphs. It is worth noting that computation times are governed by the competing influences of the number of time steps (decreasing with Δt) and the average number of Schwarz iterations per time step (increasing with Δt). Numerical experiments show that the optimal time step is close to the characteristic ratio of the local mesh size around the fault to the S-wave velocity ($V_S = \sqrt{G/\rho}$), but that accuracy remains acceptable for larger values of Δt (see [6] for a more detailed discussion in the anti-plane case).

Fig. 2 illustrates the ability of the numerical scheme to capture the characteristics of the (analytical) solution, i.e. exponential growth of the slip rate on Γ. The evolution of the logarithm of slip rate at the center of Γ, i.e. $t \mapsto \log([\dot{\boldsymbol{u}}_t(t, 0, 0)])$, is depicted. As in the anti-plane case [6], the solution follows the well-known exponential growth of the initiation pattern. The solution converges for $\Delta t \leqslant 0.1$, showing that the numerical algorithm based on Newmark time-stepping scheme and Schwarz method is efficient in capturing time instabilities, when the solution grows exponentially. Indeed, the Newmark scheme with parameters $\beta = 1/4$ and $\gamma = 1/2$, also called average acceleration method, is known to be unconditionally stable and non-dissipative (but some numerical dispersion can be observed for large time steps).

We also tested the ability of the numerical scheme to conserve the system's total energy, i.e. the sum of kinetic, potential and frictional energies:

$$\mathcal{E}(t) = \mathcal{E}_c(t) + \mathcal{E}_p(t) + \mathcal{E}_f(t) = \frac{1}{2}\int_\Omega \rho(|\dot{\boldsymbol{u}}(t)|^2 - |\dot{\boldsymbol{u}}_1|^2)\mathrm{d}\Omega + \frac{1}{2}\int_\Omega \mathcal{C}\varepsilon(\boldsymbol{u}(t)) : \varepsilon(\boldsymbol{u}(t))\mathrm{d}\Omega - \int_\Gamma \sigma_n^p F(|[\boldsymbol{u}_t(t)]|)\,\mathrm{d}\Gamma,$$

where F is an antiderivative of μ with respect to the slip s. Theoretically, the total energy $\mathcal{E}$ should be constant in time ($\mathcal{E}(t) \equiv 0$). Fig. 3 shows that it is quite stable for $\Delta t = 0.025$, proving very little numerical dissipation. In conclusion, the numerical scheme (Newmark time-stepping and Schwarz method) is satisfactorily conservative if the time step is not too large.

6.2. Normal stress variations with constant friction coefficient

Here we investigate slip instabilities triggered by normal stress variations. Note that time-dependent values of normal stress occur on non-planar or non-vertical fault geometries, and for heterogenous material properties as well. The following test should help us check the ability of the numerical scheme to account for the coupling between slip and normal stress on the fault. To this end and in contrast with the previous section (Section 6.1), the friction coefficient is taken constant:

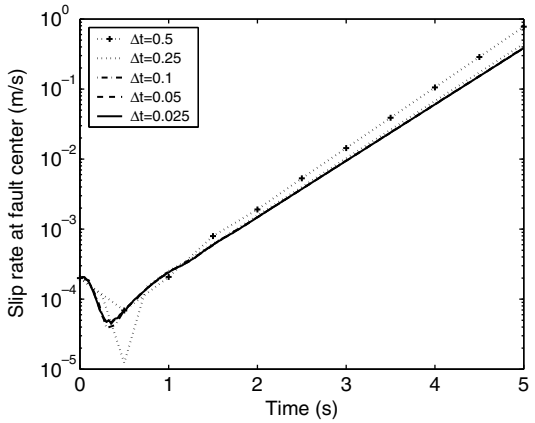

Fig. 2. Evolution of the logarithm of the slip rate at fault center, for six different values of Δt. Note that the numerical scheme is efficient in capturing unstable solutions (*i.e.* with an exponential growth in time).

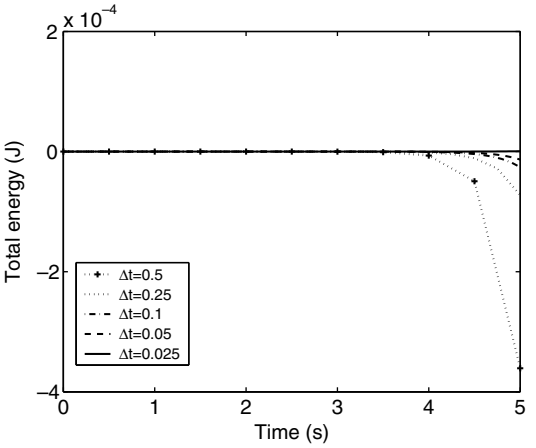

Fig. 3. Evolution of the renormalized total energy for each value of Δt.

$$\mu(\boldsymbol{x}, s) \equiv \mu$$

with $\mu = 0.4$, hence the physical model does not exhibit any slip weakening as in (39). In the following numerical tests the fault is made of 160 edges ($h = 0.00625$ locally), and the time step is fixed at $\Delta t = 0.005$.

In the previous tests of Section 6.1, the initial conditions (40) were chosen such that the solution does not exhibit any variation of normal stress on the fault. Here we have imagined a configuration in which the normal stress cannot be constant during the slip event. For that we have considered a plane wave, i.e. a special solution $\tilde{\boldsymbol{u}}$ of (1) in $\mathbb{R}^2$, given by

$$\tilde{\boldsymbol{u}}(t, \boldsymbol{x}) = \Phi((\boldsymbol{x} - \boldsymbol{x}_0) \cdot \boldsymbol{m} - V_P t)\boldsymbol{m}$$

with $\Phi : \mathbb{R} \to \mathbb{R}$ a smooth scalar function and $V_P = \sqrt{(\lambda + 2G)/\rho}$. We have chosen $\Phi(z) = V_0 \exp(z^2/(\alpha^2 - z^2))$ if $0 \leqslant |z| < \alpha$, and $\Phi(z) = 0$ if $|z| \geqslant \alpha$, with $\alpha = 0.2$ and $V_0 = 10^{-4} V_P$, $V_P = \sqrt{3}$, $\boldsymbol{m} = (\frac{1}{\sqrt{2}}, \frac{-1}{\sqrt{2}})$. This special solution corresponds to a plane wave (P-wave) of velocity V_P, which directing vector $\boldsymbol{m}$ makes an angle of 45° with respect to Γ, being driven through the medium from the top left corner of the domain Ω.

The initial conditions are $\boldsymbol{u}_0 = \tilde{\boldsymbol{u}}(0)$ and $\boldsymbol{u}_1 = \dot{\tilde{\boldsymbol{u}}}(0)$, and the P-wave is prescribed through the boundary conditions on $\Gamma_e = \partial\overline{\Omega}$, i.e. $\boldsymbol{u}_{|\Gamma_e}(t) = \tilde{\boldsymbol{u}}_{|\Gamma_e}(t)$. The point $\boldsymbol{x}_0$ was chosen such that, at $t = 0$, the incident wave has not yet touched the fault, i.e. $\boldsymbol{u}_0 = \boldsymbol{u}_1 = 0$ on Γ. The pre-stress components on the fault are $\sigma_t^p(x) = -4.0$ and $\sigma_n^p(x) = -10.0$. Since these values verify $\sigma_t^p = \mu\sigma_n^p$, and the initial over-stress $\boldsymbol{\sigma}(\boldsymbol{u}_0)$ is vanishing on Γ, the fault is at the rupture level everywhere at the initial time. Soon after $t = 0$, the P-wave touches the left tip of the fault and generates a stress perturbation on the fault. In contrast with the previous situation, described in Section 6.1, here we expect the normal stress to vary during the slip event generated by the incident P-wave.

The slip rate $[\boldsymbol{u}_t]$, together with the normal and tangential over-stresses on Γ ($\sigma_n(\boldsymbol{u})$ and $\boldsymbol{\sigma}_t(\boldsymbol{u})$ respectively), are plotted against the time and the distance along fault in Fig. 4. One can see a slip patch propagating along Γ

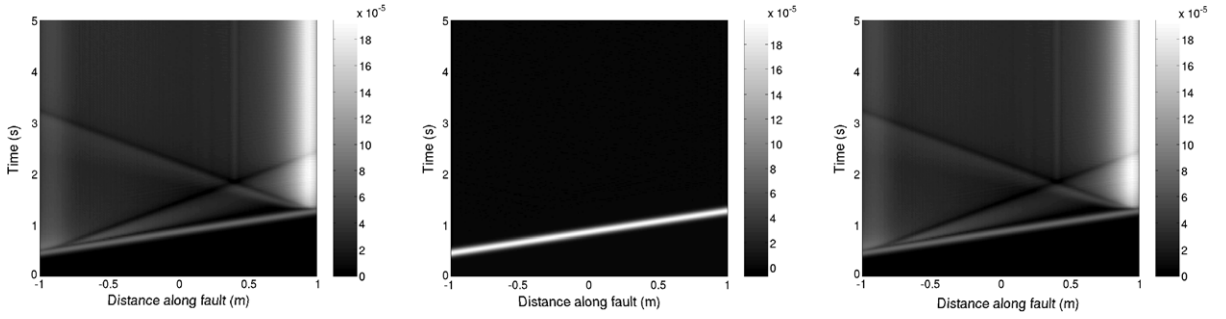

Fig. 4. Time evolution of the slip rate $[\boldsymbol{u}_t]$ (left), normal over-stress $\sigma_n(\boldsymbol{u})$ (center) and tangential over-stress $\boldsymbol{\sigma}_t(\boldsymbol{u})$ (right) on the fault Γ.

from left to right. The P-wave was chosen so that the fault is unloaded. Note that the normal stress $\sigma_n(\tilde{\boldsymbol{u}})$ generated by the P-wave is positive, so that it tends to decrease the compressive (negative) total normal stress $\boldsymbol{\sigma}_n^{\mathrm{p}} + \sigma_n(\boldsymbol{u})$ applied on the fault. Also, the fault's equilibrium is changed at the end of the simulation, with a (static) total tangential stress $\boldsymbol{\sigma}_t^{\mathrm{p}} + \boldsymbol{\sigma}_t(\boldsymbol{u})$ lower (in absolute value) than the initial stress $\boldsymbol{\sigma}_t^{\mathrm{p}}$. Note that the convention we used on the sign of the stresses is not the one usually used in seismology. Other interesting features can be observed from the shear stress evolution. First, both a P-wave and an S-wave propagate from the left fault tip (they can be observed on the right part of Fig. 4). Also, an S-wave is emitted from the right fault tip as soon as it is reached by the P-wave. The third feature is the slip induced by the S-waves interference. Fig. 5 shows two snapshots of the velocity field, before the wave has touched the fault Γ at $t = 0.4$ s, and then as the wave is passing through the fault at $t = 1.0$ s.

To point out the influence of normal stress variations on the fault's behavior, another P-wave is considered, of opposite sign (i.e. $V_0 = -10^{-4} V_{\mathrm{P}}$), arriving from the bottom left corner of the model. Unlike the first one, the second P-wave corresponds to a loading process on the fault. The differences between the two simulations are illustrated in Fig. 6, where the slip rate $[\boldsymbol{u}_t]$ and the normal and tangential over-stresses ($\sigma_n(\boldsymbol{u})$ and $\boldsymbol{\sigma}_t(\boldsymbol{u})$ respectively) are plotted against the time at the center of Γ. In this second simulation, the slip rate (on the left part of the figure) is much smaller because the total normal stress $\sigma_n^{\mathrm{p}} + \sigma_n(\boldsymbol{u})$ (middle) applied on Γ is more compressive than the pre-stress σ_n^{p}, and consequently, the shear stress drop is much smaller (right part of the figure). To analyze these differences, we denote by $\tilde{\sigma}_t = \sigma_t(\tilde{\boldsymbol{u}})$ and $\tilde{\sigma}_n = \sigma_n(\tilde{\boldsymbol{u}})$ the stresses generated by the first P-wave. With our choice of incident angle (45°) and with all elastic parameters equal to 1, we have $|\tilde{\sigma}_t|/|\tilde{\sigma}_n| = 0.5$, with $\tilde{\sigma}_t < 0$ (shear loading) and $\tilde{\sigma}_n > 0$ (decompression). In the second simulation, the absolute values are unchanged, but the normal stress is negative (compression). Hence, the resulting potential stress drop $|\tilde{\sigma}_t - \mu\tilde{\sigma}_n|$ takes the following values at each sliding point: $|-0.5\tilde{\sigma}_n - \mu\tilde{\sigma}_t| = 0.9|\tilde{\sigma}_n|$ for the unloading wave, $|0.5\tilde{\sigma}_n - \mu\tilde{\sigma}_t| = 0.1|\tilde{\sigma}_n|$ for the loading one. Note that these values are not the values observed on the figures (since they do not take the fault into account). We recall that the potential stress drop is the difference between the applied shear stress (applied tangential stress) and shear strength (static threshold corresponding to the applied normal stress). Hence the slip amplitude on Γ is expected to be larger for the unloading wave

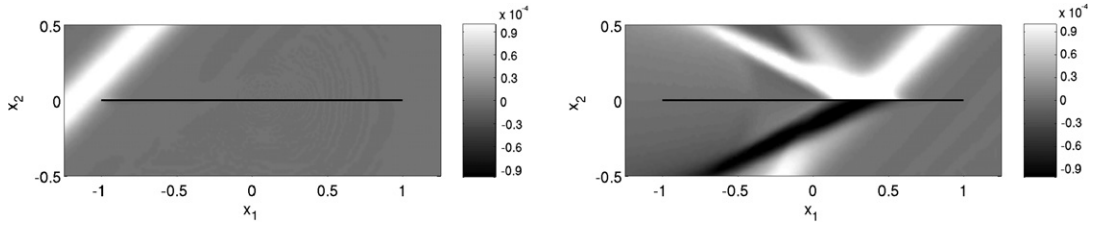

Fig. 5. Two snapshots of the tangential component of velocity $\dot{u}_t(t, x_1, x_2)$, at $t = 0.4$s before the wave has touched the fault Γ (left), and at $t = 1.0$ s as the wave is passing through it (right).

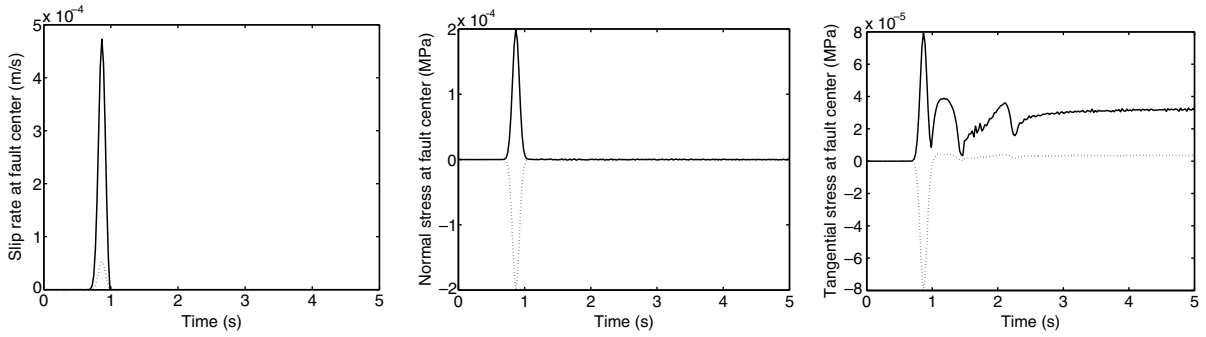

Fig. 6. Time evolution of the slip rate $[\boldsymbol{u}_t]$ (left), of the normal over-stress $\sigma_n(\boldsymbol{u})$ (center) and of the tangential over-stress $\boldsymbol{\sigma}_t(\boldsymbol{u})$ (right) at the center $(0, 0)$ of Γ for the unloading P-wave (solid lines) and for the loading P-wave (dashed lines).

than for the loading one. Two very different behaviours can be observed in Fig. 6: first, as the prescribed P-wave passes through Γ, one observes the expression of the friction law ($\sigma_t(\boldsymbol{u}) = \mu\sigma_n(\boldsymbol{u})$); then, in the absence of sliding, one can see the two travelling shear waves (the first one emitted from the left fault edge where rupture starts, the second one emitted from the right edge where rupture stops).

6.3. Application to earthquake dynamics on complex fault geometries

Numerical simulations on segmented or branched fault geometries are of great interest to understand earthquake physics. Branched fault systems are quite common in the real world, and have been widely studied through numerical modelling. We refer to some theoretical work about rupture directivity [22] and the influence of pre-stress state and rupture velocity [15,30], and to some models of the 1999 Hector Mine earthquake [38] or the 2002 Denali earthquake [8,39].

Here, we use our numerical method to compute source dynamics phenomena on a complex and realistic fault model (represented in Fig. 7). The fault system is made of one planar fault (segments 1, 2 and 3) and a lateral branch (segment 4). Note that the branching point A needs a particular treatment concerning the velocity components and the choice of the normal vector. In this "triple" point, there are three velocity vectors associated to the three sides of Γ denoted i, ii and iii (see Fig. 7). For the jumps between i and ii (resp. ii and iii, i and iii), we chose the normal of segment 2 (resp. 3, 4).

To model the evolution of the system, we need to refine the mesh around Γ, and in particular at the branching point A, and to compute a large number of time steps. To meet these requirements without increasing computation times too much, we used the coupling strategy of [46], that is, the computational domain $\overline{\Omega}$ is restricted to the close vicinity of Γ and embedded in a finite difference grid (i.e. explicit time-stepping and structured mesh) which extends in the exterior domain (see Fig. 8). The finite difference grid spacing is $dl = 500$ m; the finite element mesh coincides with this grid on their common interface, and it is refined so that the local mesh size is $dl/20$ at the branching point and $dl/10$ at the tips.

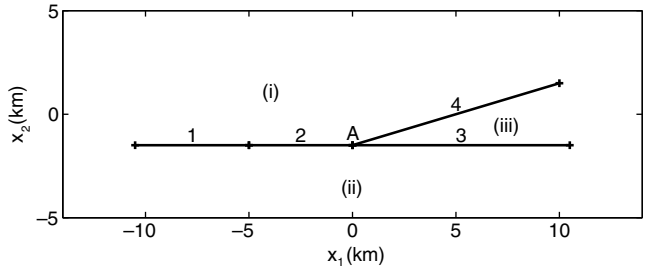

Fig. 7. Geometry of the modeled fault system.

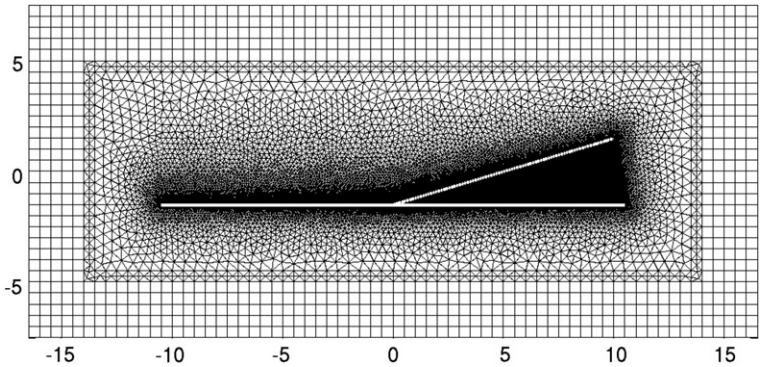

Fig. 8. Hybrid finite element–finite difference scheme [46]. The unstructured FE mesh around the fault is embedded in a FD grid (with an explicit time-stepping) efficient for wave propagation. Note that the FE nodes and the FD grid points coincide in the overlapping domain.

6.3.1. Supershear transition on a branched fault

The parameters are chosen to be physically relevant: $\rho = 3000.0\ \mathrm{kg/m^3}$, $G = \lambda = 27.0$ GPa, and the slip weakening friction law, given by (39), is piecewise linear. We performed two simulations. The physical parameters are described on Table 1; the only difference between the two simulations is the static threshold μ_s on segment 2, whose values are chosen so that segment 2 is more resistant to rupture in the second simulation. The pre-stress was chosen to be $\sigma_{11}^p = \sigma_{22}^p = -300$ MPa and $\sigma_{12}^p = -150$ MPa, such that only the first segment is initially ready to slip (i.e. $\sigma_t^p = \mu_s \sigma_n^p$ at all points of segment 1). The pre-stress is then resolved into different shear and normal components based on the fault orientation, which explains the different values of $|\sigma_n^p|$ and $|\sigma_t^p|$ on segment 4. Note that different friction coefficients were chosen on segment 4, not for computational reasons, but to avoid negative values of stress drop (since we deal in this paper with slip-weakening friction).

To compare the two numerical simulations, we show in Fig. 9 10 snapshots of the first component of the velocity field. In both simulations, the initial (small) perturbation, represented in the first snapshots at the top, is given by

$$\boldsymbol{u}_0 \equiv 0, \quad \boldsymbol{u}_1(x_1, x_2) = (\varphi_\alpha(x_1^2 + x_2^2), 0),$$

where φ_α is the same gaussian-like function as in (40). Hence, the support of the initial perturbation is concentrated near segment 1, which is very close to failure, so that rupture initiates quickly. The initiation (nucleation) phase, observed on the first three snapshots on segment 1, is characterized by a self-similar shape and an exponential growth in time. Since segment 2 is more resistant in the second simulation, the phase of rupture propagation is slightly delayed, so that the initiation phase is prolonged.

Afterwards, the two simulations are quite different, as illustrated in Fig. 9: in the first case, transition to supershear rupture velocity occurs on segment 2 and a Mach cone shear wave (S-wave) pattern can be seen behind the rupture front, whereas the characteristic pattern of sub-Rayleigh rupture propagation is observed in the second case (snapshots 4–5). The difference between the two simulations can be explained through a supershear transition criterion. Following [2,9], on each segment, we define the parameter S as follows:

$$S = \frac{\mu_s \sigma_n^p - \sigma_t^p}{\sigma_t^p - \mu_d \sigma_n^p}.$$

The values of parameter S on each segment are described in Table 1. The behavior of each fault segment is partly governed by the following supershear transition criterion (S-criterion, see [2,9]) on the rupture velocity V_{rupture}. First, let us denote by V_S the S-wave velocity, by V_{Rayleigh} the Rayleigh velocity ($V_{\mathrm{Rayleigh}} \simeq 0.92 V_S$), and let $S_c \simeq 1.63$ be the critical value of the parameter S for supershear rupture propagation to take place. Then the S-criterion can be formulated as:

$$\begin{aligned} &\text{If } S > S_c, \text{then } V_{\mathrm{rupture}} \lesssim V_{\mathrm{Rayleigh}} \ (\text{sub-Rayleigh propagation}). \\ &\text{If } S < S_c, \text{then supershear transition } (V_{\mathrm{rupture}} > V_S) \text{ can occur.} \end{aligned} \tag{41}$$

If we check now the values of parameter S in Table 1, we see that the supershear transition criterion (41) can explain the qualitative difference between the two configurations: segment 2 is eligible for supershear transition in the first simulation, but is not in the second one.

Let us go back to Fig. 9. As rupture approaches the branching point A (see Fig. 7), the segments 3 and 4 are in competition for rupture. In the first simulation (at left), the rupture arriving supershear from segment 2 just

Table 1
Columns 2–4: physical parameters used for both simulations on the fault model described in Fig. 7 (the only difference is the value of the static threshold μ_s on segment 2). Columns 5–6: normal and tangential pre-stresses. Column 7: parameter S for the supershear transition criterion

Segment	μ_s	μ_d	D_c (m)	$\lvert\sigma_n^p\rvert$ (MPa)	$\lvert\sigma_t^p\rvert$ (MPa)	S
1	0.5	0.46	0.5	300.0	150.0	0.0
2	0.51/0.57	0.46	0.5	300.0	150.0	0.25/1.75
3	0.51	0.46	0.5	300.0	150.0	0.25
4	0.33	0.28	0.5	382.57	125.23	0.056

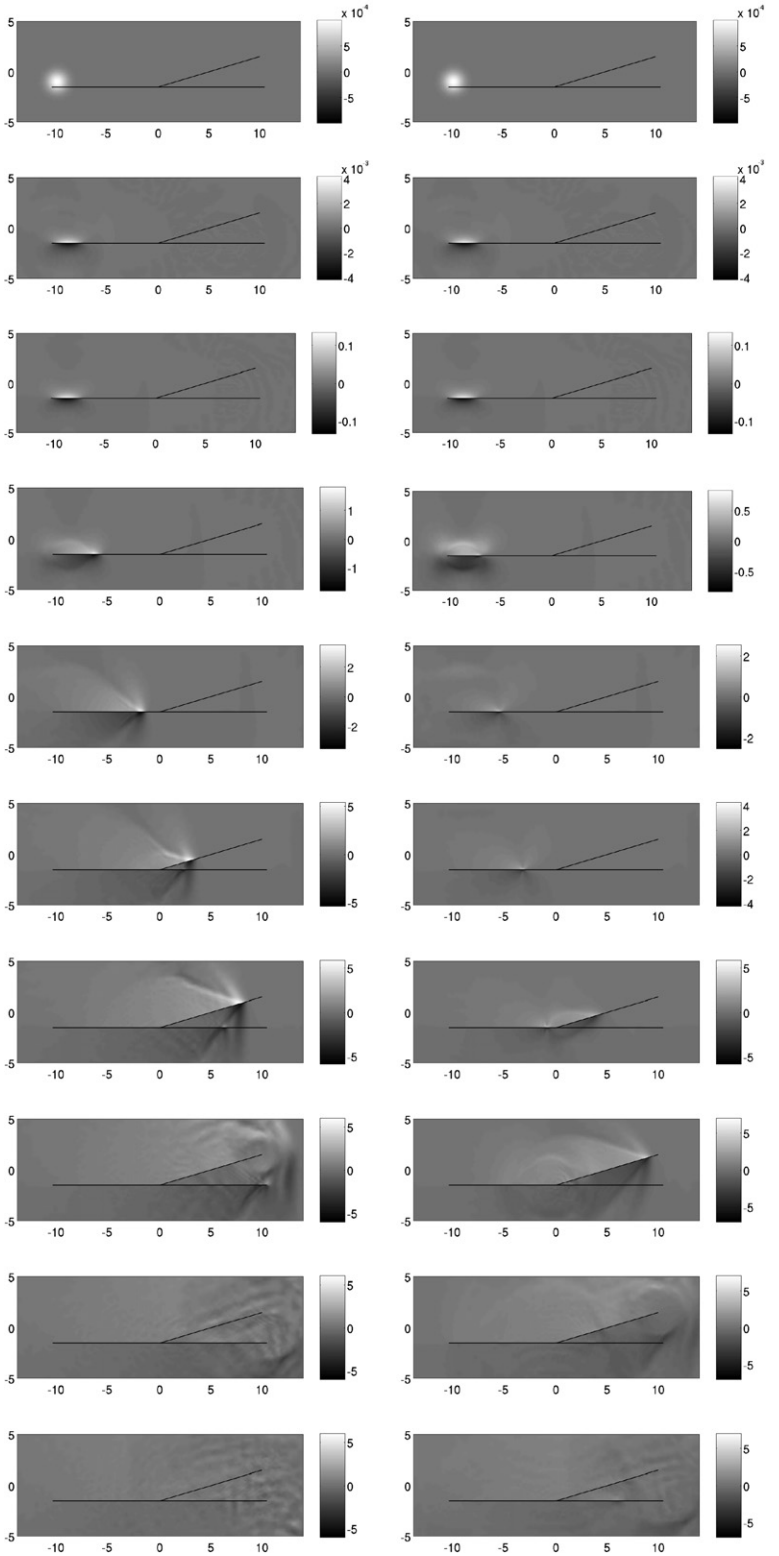

Fig. 9. Supershear transition. Evolution of the velocity field $(x_1, x_2) \to \dot{u}_1(t, x_1, x_2)$ (from top to bottom) for the two configurations described in Table 1 (the first one at left and the second one at right). The delay between two consecutive snapshots is $30\Delta t \simeq 1$ s. Note that the nature of the arriving rupture on segment 2 conditions rupture history on segments 3 and 4.

propagates further on segment 4 with a supershear velocity, so that segment 3 is unloaded. However, the strong cone wave emitted by the rupture on segment 4 generates a slip pulse on segment 3 (snapshots 6–7 at left). In the second simulation, because of the stress field created by sub-Rayleigh rupture propagation on segment 2, rupture literally jumps on segment 4 (snapshot 7 at right), where supershear transition occurs. A second rupture nucleates at the beginning of segment 4, while the rupture front on segment 2 is 3 km behind the branching point. Note that such a discontinuous rupture process was found in a model of the 2002 Denali earthquake [39]. Unlike the first simulation, the cone wave is not strong enough to trigger segment 3, which remains totally inhibited (snapshot 8 at right). These different features illustrate an important issue: the nature of the arriving rupture on segment 2 conditions rupture history on segments 3 and 4.

Some predictions can also be derived from the supershear transition criterion (41) concerning the rupture path beyond point A. From Table 1, we see that the value of S is larger on segment 3 than on segment 4, which means that segment 3 requires more energy to break, hence the rupture path is more likely to follow segment 4. And finally, the S-criterion shows that supershear transition should occur on segment 4. All these predictions are in agreement with our numerical experiments.

6.3.2. Rupture path on a branched fault

The preceding two simulations concern a very special case, since the S value is close to 0 on branch 4, so that the rupture is expected to run suddenly along this branch, with the rupture velocity jumping rapidly to P-wave speed. We consider here a case where the rupture velocity never exceeds Rayleigh speed (which is a less favorable case to resolve a rupture propagation, hence more interesting to test our numerical method). Such cases are considered in [30] (using a boundary integral equation method) where the rupture path is studied with respect to three parameters: the angle formed by segments 3 and 4, the pre-stress orientation and the location of the nucleation zone (which governs the rupture velocity when reaching the branching point). The geometry of Fig. 7 is very close to one of the cases studied in [30]. The parameters, given in Table 2, are homogeneous, except on segment 1 where the rupture initiates. The pre-stress is given by the following relations: $\sigma_{22}^{\mathrm{p}} = -300$ MPa, $\sigma_{12}^{\mathrm{p}}/\sigma_{22}^{\mathrm{p}} = 0.24$ and $\sigma_{11}^{\mathrm{p}}/\sigma_{22}^{\mathrm{p}} = 1.0$ (first case) or 2.0 (second case). Again, the pre-stress is then resolved into different shear and normal components based on the fault orientation, which explains the different values of $|\sigma_n^{\mathrm{p}}|$ and $|\sigma_t^{\mathrm{p}}|$ (hence S) on segment 4.

These two simulations are illustrated in Fig. 10. The rupture initiates on segment 1, as expected, then propagates towards point A at sub-Rayleigh speed. As the rupture reaches the branching point, the two simulations become very different: the rupture path follows segment 3 only (case 1) or segment 4 only (case 2), with sub-Rayleigh speed (case 1) or supershear speed (case 2). These results are consistent with those of [30].

6.3.3. Slip rate and stresses on a kinked fault

In the second simulation of Table 2, the segment 3 is not active, hence the fault system behaves like a simple kinked fault composed of segments 1, 2 and 4. This case was studied in [42], using a boundary integral equation method. They found a singularity at the kink (point A), which was confirmed by our computations. We performed a simulation very similar to the second configuration of Table 2, but without segment 3. Fig. 11 shows that both tangential and normal stresses are singular at the kink (according to the friction law, they are proportional at each point where the slip rate is not zero, in particular around the kink). Also, the slip profile shows an abrupt bend at the kink but remains continuous. Note that the normal stress is locally positive, which means that the fault is locally in extension and should not be ruled by friction; this physical

Table 2
Columns 2–4: physical parameters used for both simulations on the fault model described in Fig. 7 (the only difference is the ratio $\sigma_{11}^{\mathrm{p}}/\sigma_{22}^{\mathrm{p}}$, hence the pre-stress orientation). Columns 5–6: normal and tangential pre-stresses. Column 7: parameter S for the supershear transition criterion

Segment	μ_s	μ_d	D_c (m)	$\lvert\sigma_n^{\mathrm{p}}\rvert$ (MPa)	$\lvert\sigma_t^{\mathrm{p}}\rvert$ (MPa)	S
1	0.24	0.12	2.5	300.0	72.0	0.0
2	0.6	0.12	2.5	300.0	72.0	3.0
3	0.6	0.12	2.5	300.0	72.0	3.0
4	0.6	0.12	2.5	339.63/364.40	60.11/142.68	7.42/0.77

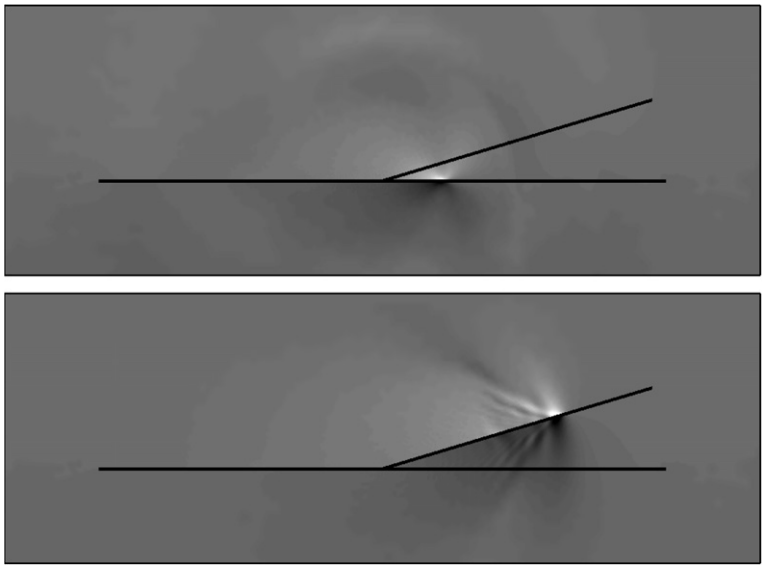

Fig. 10. Rupture path. Velocity field $(x_1, x_2) \to \dot{u}_1(t, x_1, x_2)$ at $t = 35\Delta t \simeq 1.1$ s for the two configurations described in Table 2.

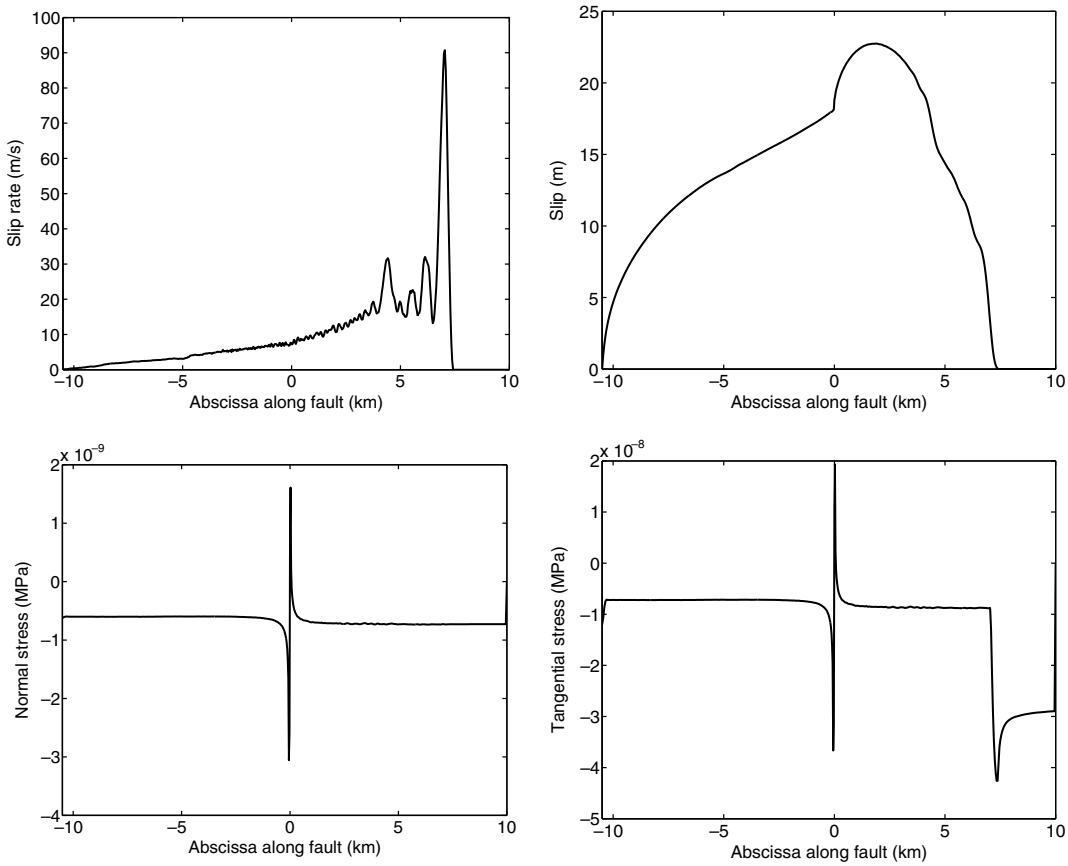

Fig. 11. Slip rate, slip, normal stress and tangential stress profiles along the kinked fault made of segments 1, 2 and 4 (see Fig. 7), projected along axis x_1 at $t = 35\Delta t \simeq 1.1$ s. The kink is located at $x_1 = 0$.

inconsistency could be partly handled by allowing separation of fault sides, or plastic deformation around the kink.

7. Conclusion

We have proposed a numerical scheme able to describe the initiation and propagation of rupture on a fault system with a complex geometry (in-plane or 3D) and to handle heterogeneous material and frictional properties. We have used the Schwarz method to solve the quasi-variational problems obtained after implicit time discretization. In fact, the problem splits into two subproblems. The first one is linear and its unknowns are related to the mesh nodes which lie inside the domain. The unknowns of the second subproblem are the degrees of freedom of the mesh nodes lying on the fault, i.e. on the domain boundary where the conditions of contact and friction are imposed. This second subproblem is nonlinear and it is handled by the same Schwarz algorithm by solving some local nonlinear subproblems of a very small size (they have three unknowns in the in-plane problem and five unknowns in the 3D problem). Hence, the global algorithm consists in solving, alternatively, one large linear subproblem and some nonlinear subproblems of a very small size.

The numerical tests illustrate the performance and convergence rate of the algorithm. Two types of instabilities are tested. First, we investigated the ability of our numerical method in capturing the instabilities generated by the slip weakening character of the friction law. The tests (convergence of Schwarz algorithm, instability capturing, energy dissipation) were performed in the in-plane configuration and show similar properties as in the anti-plane configuration [6] although the mathematical formulation is more complex (since the quasi-variational inequality cannot be associated to the minimization of the energy function). The second type of instabilities is due to normal stress variations, although the friction coefficient remains constant: the numerical scheme reveals itself to be able to account for the coupling between slip and normal stress on the fault. Finally, the numerical method was used to compute earthquake source dynamics phenomena on complex and realistic fault models (kinked or branched geometries), where both types of instabilities are present, and some relevant features are illustrated: the influence of pre-stress state on rupture path and supershear transition, and the presence of stress singularities at the kinks.

Acknowledgments

The authors acknowledge the partial support of Rhône-Alpes region through the program "Thématiques prioritaires 2003-2006". L. Badea also acknowledges the partial financial support of IMAR under the contracts CEEX05-D11-23 and CEEX06-11-12. The authors thank Pascal Favreau for helpful suggestions on relevant tests and applications to evaluate our numerical method, and for providing us with the finite difference code used in Section 6.3. We also thank David Oglesby and an anonymous reviewer for critical comments and suggestions on improving and enriching the manuscript.

Appendix

We derive in this appendix equations (25) and (26) and inequality (27), which are equivalent to problem (21) and (22) (see Section 5).

The first equation is obtained from (21) by taking $\boldsymbol{v}_{2i} \in \mathbf{V}_{2i}^h$ such that $\delta_{v_i}^n = 0, \eta_{v_i}^n = r + \bar{r}, \eta_{v_i}^t = s$ and $\delta_{v_i}^t = t$, for any $\bar{r} \in \mathbb{R}$. In this way we have,

$$b(\tilde{\boldsymbol{u}}_{2i}^{n+1,m+1}, \boldsymbol{n}_i\phi_i^+ + \boldsymbol{n}_i\phi_i^-) + \left(\frac{\Delta t}{2}\right)^2 a(\tilde{\boldsymbol{u}}_{2i}^{n+1,m+1}, \boldsymbol{n}_i\phi_i^+ + \boldsymbol{n}_i\phi_i^-) = F_k(\boldsymbol{n}_i\phi_i^+ + \boldsymbol{n}_i\phi_i^-),$$

and using (24), we get Eq. (25), that is:

$$a_{nn}^+ r + b_{nt}^+ s + b_{nt}^- t = d_n^+,$$

where

$$a_{nn}^{+} := \frac{1}{2} b(\boldsymbol{n}_i\phi_i^{+} + \boldsymbol{n}_i\phi_i^{-}, \boldsymbol{n}_i\phi_i^{+} + \boldsymbol{n}_i\phi_i^{-}) + \frac{1}{2}\left(\frac{\Delta t}{2}\right)^2 a(\boldsymbol{n}_i\phi_i^{+} + \boldsymbol{n}_i\phi_i^{-}, \boldsymbol{n}_i\phi_i^{+} + \boldsymbol{n}_i\phi_i^{-}),$$

$$b_{nt}^{+} := \frac{1}{2}\left(\frac{\Delta t}{2}\right)^2 a(\boldsymbol{t}_i\phi_i^{+} + \boldsymbol{t}_i\phi_i^{-}, \boldsymbol{n}_i\phi_i^{+} + \boldsymbol{n}_i\phi_i^{-}),$$

$$b_{nt}^{-} := \frac{1}{2}\left(\frac{\Delta t}{2}\right)^2 a(\boldsymbol{t}_i\phi_i^{+} - \boldsymbol{t}_i\phi_i^{-}, \boldsymbol{n}_i\phi_i^{+} + \boldsymbol{n}_i\phi_i^{-}),$$

$$d_{n}^{+} := F_k(\boldsymbol{n}_i\phi_i^{+} + \boldsymbol{n}_i\phi_i^{-}) - b(\hat{\tilde{\boldsymbol{u}}}_{2i}^{n+1,m+1}, \boldsymbol{n}_i\phi_i^{+} + \boldsymbol{n}_i\phi_i^{-}) - \left(\frac{\Delta t}{2}\right)^2 a(\hat{\tilde{\boldsymbol{u}}}_{2i}^{n+1,m+1}, \boldsymbol{n}_i\phi_i^{+} + \boldsymbol{n}_i\phi_i^{-}). \tag{42}$$

The second equation is obtained from (21) by taking $\boldsymbol{v}_{2i} \in \mathbf{V}_{2i}^h$ with $\delta_{v_i}^n = 0, \eta_{v_i}^n = r_i^{m+1}, \eta_{v_i}^t = s + \bar{s}$ and $\delta_{v_i}^t = t$, for any $\bar{s} \in \mathbb{R}$. We get

$$b(\tilde{\dot{\boldsymbol{u}}}_{2i}^{n+1,m+1}, \boldsymbol{t}_i\phi_i^{+} + \boldsymbol{t}_i\phi_i^{-}) + \left(\frac{\Delta t}{2}\right)^2 a(\tilde{\dot{\boldsymbol{u}}}_{2i}^{n+1,m+1}, \boldsymbol{t}_i\phi_i^{+} + \boldsymbol{t}_i\phi_i^{-}) = F_k(\boldsymbol{t}_i\phi_i^{+} + \boldsymbol{t}_i\phi_i^{-}),$$

and then we derive Eq. (26), that is:

$$b_{nt}^{+} r + a_{tt}^{+} s + a_{tt}^{-} t = d_t^{+},$$

where

$$a_{tt}^{+} := \frac{1}{2} b(\boldsymbol{t}_i\phi_i^{+}\boldsymbol{t}_i\phi_i^{-}, \boldsymbol{t}_i\phi_i^{+} + \boldsymbol{t}_i\phi_i^{-}) + \frac{1}{2}\left(\frac{\Delta t}{2}\right)^2 a(\boldsymbol{t}_i\phi_i^{+} + \boldsymbol{t}_i\phi_i^{-}, \boldsymbol{t}_i\phi_i^{+} + \boldsymbol{t}_i\phi_i^{-}),$$

$$a_{tt}^{-} := \frac{1}{2} b(\boldsymbol{t}_i\phi_i^{+} - \boldsymbol{t}_i\phi_i^{-}, \boldsymbol{t}_i\phi_i^{+} + \boldsymbol{t}_i\phi_i^{-}) + \frac{1}{2}\left(\frac{\Delta t}{2}\right)^2 a(\boldsymbol{t}_i\phi_i^{+} - \boldsymbol{t}_i\phi_i^{-}, \boldsymbol{t}_i\phi_i^{+} + \boldsymbol{t}_i\phi_i^{-}),$$

$$d_{t}^{+} := F_k(\boldsymbol{t}_i\phi_i^{+} + \boldsymbol{t}_i\phi_i^{-}) - b(\hat{\tilde{\boldsymbol{u}}}_{2i}^{n+1,m+1}, \boldsymbol{t}_i\phi_i^{+} + \boldsymbol{t}_i\phi_i^{-}) - \left(\frac{\Delta t}{2}\right)^2 a(\hat{\tilde{\boldsymbol{u}}}_{2i}^{n+1,m+1}, \boldsymbol{t}_i\phi_i^{+} + \boldsymbol{t}_i\phi_i^{-}), \tag{43}$$

and b_{nt}^{+} is given by (42).

Now, we find σ_n at node i from (22). To this end, we take $\boldsymbol{w} = \boldsymbol{w}_{2i} = \boldsymbol{w}_i^{+}\phi_i^{+} + \boldsymbol{w}_i^{-}\phi_i^{-} \in \mathbf{W}_{2i}^h$ in (22). We have $[\boldsymbol{w}_{2i} \cdot \boldsymbol{n}_i] = \delta_{w_i}^n \varphi_i$, and because $\boldsymbol{w}_{2i} \in \mathbf{W}^h$ we get $\delta_{w_i}^t = 0$. Consequently, writing

$$\sigma_n = \sum_{i=1}^{n_f} \sigma_n^i \psi_i, \tag{44}$$

where $\psi_i,\ i = 1, \ldots, n_f$, are the Lagrange multipliers with property (16), we get

$$\begin{aligned}
\delta_{w_i}^n \sigma_n^i \frac{\Delta t}{2} \int_\Gamma \varphi_i = {} & b\left(\tilde{\dot{\boldsymbol{u}}}_{2i}^{n+1,m+1}, \frac{1}{2}\delta_{w_i}^n \boldsymbol{n}_i(\phi_i^{+} - \phi_i^{-}) + \frac{1}{2}(\eta_{w_i}^n \boldsymbol{n}_i + \eta_{w_i}^t \boldsymbol{t}_i)(\phi_i^{+} + \phi_i^{-})\right) \\
& + \left(\frac{\Delta t}{2}\right)^2 a\left(\tilde{\dot{\boldsymbol{u}}}_{2i}^{n+1,m+1}, \frac{1}{2}\delta_{w_i}^n \boldsymbol{n}_i(\phi_i^{+} - \phi_i^{-}) + \frac{1}{2}(\eta_{w_i}^n \boldsymbol{n}_i + \eta_{w_i}^t \boldsymbol{t}_i)(\phi_i^{+} + \phi_i^{-})\right) \\
& - F_k\left(\frac{1}{2}\delta_{w_i}^n \boldsymbol{n}_i(\phi_i^{+} - \phi_i^{-}) + \frac{1}{2}(\eta_{w_i}^n \boldsymbol{n}_i + \eta_{w_i}^t \boldsymbol{t}_i)(\phi_i^{+} + \phi_i^{-})\right).
\end{aligned} \tag{45}$$

Moreover, condition $[\boldsymbol{\sigma}(\tilde{\dot{\boldsymbol{u}}}_{2i}^{n+1,m+1})\boldsymbol{n}] = 0$ on Γ, from (5), can be written in a weak form as

$$0 = \frac{\Delta t}{2} \int_\Gamma [\boldsymbol{\sigma}(\tilde{\dot{\boldsymbol{u}}}_{2i}^{n+1,m+1})\boldsymbol{n}] \cdot \boldsymbol{w}_{2i} = b(\tilde{\dot{\boldsymbol{u}}}_{2i}^{n+1,m+1}, \boldsymbol{w}_{2i}) + \left(\frac{\Delta t}{2}\right)^2 a(\tilde{\dot{\boldsymbol{u}}}_{2i}^{n+1,m+1}, \boldsymbol{w}_{2i}) - F_k(\boldsymbol{w}_{2i}),$$

for any $\boldsymbol{w}_{2i} \in \mathbf{U}_{2i}$ with $\delta_{w_i}^n = \delta_{w_i}^t = 0,\ i = 1, \ldots, n_f$. We conclude that

$$b\left(\tilde{\dot{\boldsymbol{u}}}_{2i}^{n+1,m+1},\frac{1}{2}(\eta_{w_i}^n\boldsymbol{n}_i+\eta_{w_i}^t\boldsymbol{t}_i)(\phi_i^+-\phi_i^-)\right)+\left(\frac{\Delta t}{2}\right)^2 a\left(\tilde{\dot{\boldsymbol{u}}}_{2i}^{n+1,m+1},\frac{1}{2}(\eta_{w_i}^n\boldsymbol{n}_i+\eta_{w_i}^t\boldsymbol{t}_i)(\phi_i^+-\phi_i^-)\right)$$
$$-F_k\left(\frac{1}{2}(\eta_{w_i}^n\boldsymbol{n}_i+\eta_{w_i}^t\boldsymbol{t}_i)(\phi_i^+-\phi_i^-)\right)=0, \tag{46}$$

and from (45) and (46) we get

$$\sigma_n^i=\frac{1}{\Delta t\int_\Gamma\varphi_i}\left\{b(\tilde{\dot{\boldsymbol{u}}}_{2i}^{n+1,m+1},\boldsymbol{n}_i\phi_i^+-\boldsymbol{n}_i\phi_i^-)+\left(\frac{\Delta t}{2}\right)^2 a(\tilde{\dot{\boldsymbol{u}}}_{2i}^{n+1,m+1},\boldsymbol{n}_i\phi_i^+-\boldsymbol{n}_i\phi_i^-)-F_k(\boldsymbol{n}_i\phi_i^+-\boldsymbol{n}_i\phi_i^-)\right\}.$$

From this equation, using again (24), we get

$$\sigma_n^i=\frac{1}{\Delta t\int_\Gamma\varphi_i}(a_{nn}^-r+b_{nt}^-s+b_{nt}^+t-d_n^-), \tag{47}$$

where

$$a_{nn}^-=\frac{1}{2}b(\boldsymbol{n}_i\phi_i^++\boldsymbol{n}_i\phi_i^-,\boldsymbol{n}_i\phi_i^+-\boldsymbol{n}_i\phi_i^-)+\frac{1}{2}\left(\frac{\Delta t}{2}\right)^2 a(\boldsymbol{n}_i\phi_i^++\boldsymbol{n}_i\phi_i^-,\boldsymbol{n}_i\phi_i^+-\boldsymbol{n}_i\phi_i^-)$$
$$d_n^-=F_k(\boldsymbol{n}_i\phi_i^+-\boldsymbol{n}_i\phi_i^-)-b(\hat{\dot{\boldsymbol{u}}}_{2i}^{n+1,m+1},\boldsymbol{n}_i\phi_i^+-\boldsymbol{n}_i\phi_i^-)-\left(\frac{\Delta t}{2}\right)^2 a(\hat{\dot{\boldsymbol{u}}}_{2i}^{n+1,m+1},\boldsymbol{n}_i\phi_i^+-\boldsymbol{n}_i\phi_i^-), \tag{48}$$

and b_{nt}^- and b_{nt}^+ are defined in (42). Now, we obtain an inequality from (21) by taking $\boldsymbol{v}_{2i}\in\mathbf{V}_{2i}^h$ with $\delta_{v_i}^n=0,\eta_{v_i}^n=r,\eta_{v_i}^t=s$ and $\delta_{v_i}^t=\bar{t}$, where $\bar{t}\in\mathbb{R}$. In this way we have,

$$\frac{1}{2}(\bar{t}-t)b(\tilde{\dot{\boldsymbol{u}}}_{2i}^{n+1,m+1},\boldsymbol{t}_i\phi_i^+-\boldsymbol{t}_i\phi_i^-)+\frac{1}{2}(\bar{t}-t)\left(\frac{\Delta t}{2}\right)^2 a(\tilde{\dot{\boldsymbol{u}}}_{2i}^{n+1,m+1},\boldsymbol{t}_i\phi_i^+-\boldsymbol{t}_i\phi_i^-)$$
$$-\frac{\Delta t}{2}\mu_{ki}(|t|)(\sigma_n^i+(\sigma^{\mathrm{p}})_n^i)(|\bar{t}|-|t|)\int_\Gamma\varphi_i\geqslant\frac{1}{2}(\bar{t}-t)F_k(\boldsymbol{t}_i\phi_i^+-\boldsymbol{t}_i\phi_i^-),$$

where we have taken into account that $|[(\dot{\boldsymbol{u}}_{2i}^{n+1,m+1})_t]|=|t|,|[(v_{2i})_t]|=|\bar{t}|$, and like in (44), we have written $\sigma_n^{\mathrm{p}}=\sum_{i=1}^{n_f}(\sigma^{\mathrm{p}})_n^i\psi_i$. The above inequality can be written as

$$\frac{1}{2}(\bar{t}-t)(b_{nt}^-r+a_{tt}^-s+a_{tt}^+t-d_t^-)-\frac{\Delta t}{2}\mu_{ki}(|t|)(\sigma_n^i+(\sigma^{\mathrm{p}})_n^i)(|\bar{t}|-|t|)\int_\Gamma\varphi_i\geqslant 0, \tag{49}$$

where b_{nt}^- is defined in (42), a_{tt}^- and a_{tt}^+ are defined in (43), and

$$d_t^-F_k(\boldsymbol{t}_i\phi_i^+-\boldsymbol{t}_i\phi_i^-)-b(\hat{\dot{\boldsymbol{u}}}_{2i}^{n+1,m+1},\boldsymbol{t}_i\phi_i^+-\boldsymbol{t}_i\phi_i^-)-\left(\frac{\Delta t}{2}\right)^2 a(\hat{\dot{\boldsymbol{u}}}_{2i}^{n+1,m+1},\boldsymbol{t}_i\phi_i^+-\boldsymbol{t}_i\phi_i^-). \tag{50}$$

Finally, from (47) and (49), we get inequality (27), that is

$$(b_{nt}^-r+a_{tt}^-s+a_{tt}^+t-d_t^-)(\bar{t}-t)-\left(a_{nn}^-r+b_{nt}^-s+b_{nt}^+t-d_n^-+(\sigma^{\mathrm{p}})_n^i\Delta t\int_\Gamma\varphi_i\right)\mu_{ki}(|t|)(|\bar{t}|-|t|)\geqslant 0,\quad\forall\bar{t}\in\mathbb{R}.$$

References

[1] B. Aagaard, Finite-element simulations of earthquakes, Ph.D. Thesis, California Institute of Technology, Pasadena, 2000.

[2] D.J. Andrews, Rupture velocity of plane strain shear cracks, J. Geophys. Res. 81 (B32) (1976) 5679–5689.

[3] H. Aochi, E. Fukuyama, M. Matsu'ura, Spontaneous rupture propagation on a non-planar fault in 3-D elastic medium, Pure Appl. Geophys. 157 (11–12) (2000) 2003–2027.

[4] H. Aochi, O. Scotti, C. Berge-Thierry, Dynamic transfer of rupture across differently oriented segments in a complex 3-D fault system, Geophys. Res. Lett. 32 (21) (2005) L21304.1–L21304.4.

[5] R. Archuleta, G. Frazier, Three-dimensional numerical simulations of dynamic faulting in a half-space, Bull. Seis. Soc. Am. 68 (1978) 541–572.

[6] L. Badea, I.R. Ionescu, S. Wolf, Domain decomposition method for dynamic faulting under slip-dependent friction, J. Comput. Phys. 201 (2004) 487–510.

[7] M. Ben Jemaa, N. Glinsky-Olivier, V.M. Cruz-Atienza, J. Virieux, S. Piperno, Dynamic non-planar crack rupture by a finite volume method, Geophys. J. Int. 171 (1) (2007) 271–285.
[8] H.S. Bhat, R. Dmowska, J.R. Rice, N. Kame, Dynamic slip transfer from the Denali to Totschunda Faults, Alaska: testing theory for fault branching, Bull. Seis. Soc. Am. 94 (2004) S202–S213.
[9] R. Burridge, Admissible speeds for plane-strain self-similar shear cracks with friction but lacking cohesion, Geophys. J. Roy. Astr. Soc. 35 (1973) 439–455.
[10] M. Campillo, I.R. Ionescu, Initiation of antiplane shear instability under slip dependent friction, J. Geophys. Res. 122 (B9) (1997) 20363–20371.
[11] V.M. Cruz-Atienza, J. Virieux, Dynamic rupture simulation of non-planar faults with a finite-difference approach, Geophys. J. Int. 158 (3) (2004) 939–954.
[12] V.M. Cruz-Atienza, J. Virieux, H. Aochi, 3D finite-difference dynamic-rupture modeling along nonplanar faults, Geophysics 72 (5) (2007) SM123–SM137.
[13] C. Dascalu, I.R. Ionescu, Slip weakening friction instabilities: eigenvalue analysis, M3AS 14 (3) (2004) 439–459.
[14] C. Dascalu, I.R. Ionescu, M. Campillo, Fault finiteness and initiation of dynamic shear instability, Earth Planet. Sci. Lett. 177 (2000) 163–176.
[15] B. Duan, D.D. Oglesby, Nonuniform prestress from prior earthquakes and the effect on dynamics of branched fault systems, J. Geophys. Res. 112 (2007) B05308.
[16] W.L. Elsworth, G.C. Beroza, Seismic evidence for an earthquake nucleation phase, Science 268 (1995) 851–855.
[17] K. Fackeldey, R. Krause, Solving frictional contact problems with multigrid efficiency, in: Proc. 16th Int. Conf. on Domain Decomposition, New York, 2005.
[18] P. Favreau, M. Campillo, I.R. Ionescu, Initiation of inplane shear instability under slip dependent friction, Bull. Seis. Soc. Am. 89 (5) (1999) 1280–1295.
[19] P. Favreau, M. Campillo, I.R. Ionescu, Initiation of instability under slip dependent friction in three dimensions, J. Geophys. Res. 107 (B7) (2002) 2147.
[20] G. Festa, J.-P. Vilotte, Influence of the rupture initiation on the intersonic transition: crack-like versus pulse-like modes, Geophys. Res. Lett. 33 (2006) L15320.
[21] G. Festa, J.-P. Vilotte, Dynamic rupture propagation and radiation along kinked faults, European Geosciences Union 2006, Geophys. Res. Abstr. 8 (2006) 06228.
[22] S. Fliss, H.S. Bhat, R. Dmowska, J.R. Rice, Fault branching and rupture directivity, J. Geophys. Res. 110 (2005) B06312.
[23] T.C. Fung, Unconditionally stable higher order Newmark methods by sub-stepping procedure, Comput. Methods Appl. Mech. Eng. 147 (1997) 61–84.
[24] R. Glowinski, Numerical Methods for Nonlinear Variational Problems, Springer, New York, 1984.
[25] R. Glowinski, G.H. Golub, G.A. Meurant, J. Périeux (Eds.), First Int. Symp. on Domain Decomposition Methods, SIAM, Philadelphia, 1988.
[26] R. Hassani, I.R. Ionescu, E. Oudet, Critical friction for wedged configurations, Int. J. Solids Struct. 44 (18–19) (2007) 6187–6200.
[27] J. Haslinger, I. Hlavácek, J. Necas, Numerical methods for unilateral problems in solid mechanics, Amsterdam, in: P.G. Ciarlet, J.L. Lions (Eds.), Handbook of Numerical Analysis, vol. IV(2), North Holland, 1996.
[28] Y. Iio, Slow initial phase of the P-wave velocity pulse generated by microearthquakes, Geophys. Res. Lett. 19 (5) (1992) 477–480.
[29] I.R. Ionescu, M. Campillo, The influence of the shape of the friction law and fault finiteness on the duration of initiation, J. Geophys. Res. 104 (B2) (1999) 3013–3024.
[30] N. Kame, J.R. Rice, R. Dmowska, Effects of prestress state and rupture velocity on dynamic fault branching, J. Geophys. Res. 108 (B5) (2003) 2265.
[31] N. Kikuchi, J.T. Oden, Contact Problems in Elasticity: A Study of Variational Inequalities and Finite Elements, SIAM, Philadelphia, 1988.
[32] R. Kornhuber, Adaptive Monotone Multigrid Methods for Nonlinear Variational Problem, Teubner, Stuttgart, 1997.
[33] T.A. Laursen, Computational Contact and Impact Mechanics, Springer, Berlin, 2002.
[34] T.A. Laursen, J.C. Simo, A continuum-based finite element formulation for the implicit solution of multibody, large deformation frictional contact problems, Int. J. Numer. Methods Eng. 36 (20) (1993) 3451–3485.
[35] A. Quarteroni, A. Valli, Domain Decomposition Methods for Partial Differential Equations, Oxford Science Publications, 1999.
[36] D.D. Oglesby, Earthquake dynamics on dip-slip faults, Ph.D. Thesis, University of California, Santa Barbara, 1999.
[37] D.D. Oglesby, R. Archuleta, S. Nielsen, Dynamics of dip-slip faulting: explorations in two dimensions, J. Geophys. Res. 105 (B6) (2000) 13643–13654.
[38] D.D. Oglesby, S.M. Day, Y.-G. Li, J.E. Vidale, The 1999 Hector Mine earthquake: the dynamics of a branched fault system, Bull. Seis. Soc. Am. 93 (6) (2003) 2459–2476.
[39] D.D. Oglesby, D. Dreger, R.A. Harris, N.A. Ratchkovski, R. Hansen, Inverse kinematic and forward dynamic models of the 2002 Denali Fault Earthquake, Alaska, Bull. Seis. Soc. Am. 94 (2004) S214–S233.
[40] M. Ohnaka, Y. Kuwakara, K. Yamamoto, Constitutive relations between dynamic physical parameters near a tip of the propagation slip during stick-slip shear failure, Tectonophysics 144 (1987) 109–125.
[41] B.F. Smith, P.E. Bjørstad, William Gropp, Domain Decomposition: Parallel Multilevel Methods for Elliptic Differential Equations, Cambridge University Press, 1996.
[42] T. Tada, T. Yamashita, The paradox of smooth and abrupt bends in two-dimensional in-plane shear-crack mechanics, Geophys. J. Int. 127 (3) (1996) 795–800.

[43] A. Toselli, O. Widlund, Domain decomposition methods: algorithms and theory, Springer Series in Computational Mathematics, vol. 34, 2004.
[44] K. Uenishi, J.R. Rice, Universal nucleation length for slip-weakening rupture instability under non-uniform fault loading, J. Geophys. Res. 108 (B1) (2003) 2042.
[45] B.I. Wohlmuth, A mortar finite element method using dual spaces for the Lagrange multiplier, SIAM J. Numer. Anal. 38 (2000) 989–1012.
[46] S. Wolf, P. Favreau, I.R. Ionescu, Finite element–finite difference coupling for wave propagation. Application to seismic rupture modeling, Eos Trans. AGU 87 (52) (2006) (Fall Meet. Suppl., Abstract S41B-1332).
[47] P. Wriggers, Computational Contact Mechanics, John Wiley & Sons, 2002.
[48] Z.H. Zong, Finite Element Procedures in Contact–impact Problems, Oxford University Press, 1993.